

Mathematical models of action potentials in the periphery and center of the rabbit sinoatrial node

H. ZHANG,¹ A. V. HOLDEN,¹ I. KODAMA,² H. HONJO,² M. LEI,¹
T. VARGHESE,³ AND M. R. BOYETT¹

¹School of Biomedical Sciences, University of Leeds, Leeds LS2 9JT, United Kingdom;

²Departments of Circulation and Humoral Regulation, Research Institute of Environmental Medicine, Nagoya University, Nagoya 464-01, Japan; and ³Institute for Mathematics and Its Application, University of Minnesota, Minneapolis, Minnesota 55455

Received 17 June 1999; accepted in final form 5 January 2000

Zhang, H., A. V. Holden, I. Kodama, H. Honjo, M. Lei, T. Varghese, and M. R. Boyett. Mathematical models of action potentials in the periphery and center of the rabbit sinoatrial node. *Am J Physiol Heart Circ Physiol* 279: H397–H421, 2000.—Mathematical models of the action potential in the periphery and center of the rabbit sinoatrial (SA) node have been developed on the basis of published experimental data. Simulated action potentials are consistent with those recorded experimentally: the model-generated peripheral action potential has a more negative takeoff potential, faster upstroke, more positive peak value, prominent phase 1 repolarization, greater amplitude, shorter duration, and more negative maximum diastolic potential than the model-generated central action potential. In addition, the model peripheral cell shows faster pacemaking. The models behave qualitatively the same as tissue from the periphery and center of the SA node in response to block of tetrodotoxin-sensitive Na⁺ current, L- and T-type Ca²⁺ currents, 4-aminopyridine-sensitive transient outward current, rapid and slow delayed rectifying K⁺ currents, and hyperpolarization-activated current. A one-dimensional model of a string of SA node tissue, incorporating regional heterogeneity, coupled to a string of atrial tissue has been constructed to simulate the behavior of the intact SA node. In the one-dimensional model, the spontaneous action potential initiated in the center propagates to the periphery at ~0.06 m/s and then into the atrial muscle at 0.62 m/s.

heart; pacemaking; regional differences; computer modeling

THE RHYTHMIC BEATING of the heart is the result of action potentials initiated in the pacemaker of the heart, the sinoatrial (SA) node. Mathematical models of the electrical activity of the SA node of the rabbit (the species for which most data have been obtained) have been produced. The first models were produced by Yanagihara et al. (61) and Noble and Noble (49), and subsequent models were developed from the earlier models (13, 18, 59).

All the above models are of a typical SA node action potential. However, the SA node, functionally, anatomically, and electrophysiologically, is not homogeneous.

In the rabbit the SA node measures ~8 mm × ~10 mm (5). In the vertical direction it is bounded by the superior and inferior venae cavae, and in the horizontal direction it is bounded by the crista terminalis (a thick bundle of atrial muscle) and the interatrial septum. The action potential is initiated in a small part of the SA node, the leading pacemaker site. Normally, the leading pacemaker site is approximately midway between the two venae cavae and 1–2 mm from the crista terminalis (3). This region is referred to as the center of the SA node. From the leading pacemaker site in the center, the action potential propagates to the periphery of the SA node and then onto the atrial muscle of the crista terminalis. Conduction toward the interatrial septum is blocked (3). The periphery of the SA node (the region of the SA node close to the crista terminalis) is referred to by some authors as perinode or transitional tissue. Although the principal function of the periphery of the SA node is to conduct the action potential from the leading pacemaker site in the center to the atrial muscle, the periphery does show pacemaker activity. In response to a variety of interventions, for example, autonomic nerve stimulation, the leading pacemaker site shifts from the center, and in many cases it shifts toward the periphery (53); the pacemaker activity of the periphery of the SA node is, therefore, important physiologically. Most work on regional differences in the SA node has been carried out on tissue around the leading pacemaker site midway between the venae cavae and has focused on peripheral-central differences (little is known about the tissue from the more superior and inferior regions and also toward the interatrial septum). There are important anatomic differences; for example, in the center the cells are smaller and have fewer and more poorly organized myofilaments than in the periphery (3). There are electrophysiological differences; these have been studied in the intact SA node or in small balls of tissue from different regions of the SA node. In the

Address for reprint requests and other correspondence: M. R. Boyett, School of Biomedical Sciences, University of Leeds, Leeds LS2 9JT, UK (E-mail: m.r.boyett@leeds.ac.uk).

The costs of publication of this article were defrayed in part by the payment of page charges. The article must therefore be hereby marked "advertisement" in accordance with 18 U.S.C. Section 1734 solely to indicate this fact.

periphery the takeoff potential is more negative, the action potential upstroke velocity is higher, the action potential is shorter, the maximum diastolic potential (also resting potential in quiescent tissue) is more negative, and the intrinsic pacemaker activity is paradoxically faster than in the center (33). Ion channel block has different effects in the different regions: block of tetrodotoxin-sensitive Na^+ current (i_{Na}), 4-aminopyridine (4-AP)-sensitive transient outward current (i_{to}), or hyperpolarization-activated current (i_{p}) has a greater effect in the periphery, whereas block of L-type Ca^{2+} current ($i_{\text{Ca,L}}$) or rapid delayed rectifying K^+ current ($i_{\text{K,r}}$) has a greater effect in the center (6, 32, 33, 45). These differences in the response to ion channel block suggest regional differences in ionic currents. Single cells have not been isolated from different regions of the SA node to confirm this. However, we isolate single cells from the whole of the SA node and then distinguish between cells on the basis of cell capacitance (C_{m}), a measure of cell size, which is known to vary between the periphery and the center (see above) (27, 28, 36, 39). The action potential characteristics vary with C_{m} in a manner consistent with the regional differences (see above) (27). For example, in large cells with a high C_{m} (presumably from the periphery) the upstroke velocity is high, whereas in small cells with a low C_{m} (presumably from the center) the upstroke velocity is low (27). We have measured the density of some ionic currents; whereas the density of $i_{\text{Ca,L}}$ is not significantly different in cells of different size, the densities of i_{Na} , i_{to} , $i_{\text{K,r}}$, $i_{\text{K,s}}$, and i_{f} are greater in larger cells (27, 28, 36, 39; $i_{\text{K,r}}$ and $i_{\text{K,s}}$ data from unpublished observations).

Models incorporating regional differences within the SA node have been developed (49, 60). However, the models were based on speculation because of the absence of data on regional differences in ionic currents. The aim of the present study was to develop, on the basis of the evidence reviewed above, biophysically detailed models of action potentials in the periphery and center of the rabbit SA node.

Glossary

| | |
|---|---|
| 4-AP | 4-Aminopyridine |
| AM | Atrial muscle |
| APD | Action potential duration |
| CL | Spontaneous cycle length |
| C_{m} | Cell capacitance |
| $C_{\text{m}}^{\text{a}}(x)$, $C_{\text{m}}^{\text{s}}(x)$ | Capacitance of atrial muscle cell or SA node cell in one-dimensional model of intact SA node at distance x from center of SA node |
| d_{L} , d_{T} | Activation variables for $i_{\text{Ca,L}}$ and $i_{\text{Ca,T}}$ |
| d_{NaCa} | Denominator constant for i_{NaCa} |
| dV/dt_{max} | Maximum upstroke velocity of action potential |
| D^{a} , D^{s} | Diffusion coefficient between atrial muscle cells or SA node cells in |

$E_{\text{K,s}}$
 E_{Na} , E_{Ca} , E_{K}

$E_{\text{Ca,L}}$, $E_{\text{Ca,T}}$

F

$F_{\text{K,r}}$

F_{Na}

f_{L} , f_{T}

g_{p} , g_{c}

$g^{\text{a}}(x)$, $g^{\text{s}}(x)$

g_{Na}

$g_{\text{Ca,L}}$, $g_{\text{Ca,T}}$

g_{to} , g_{sus}

$g_{\text{K,r}}$, $g_{\text{K,s}}$

$g_{\text{f,Na}}$, $g_{\text{f,K}}$

$g_{\text{b,Na}}$, $g_{\text{b,Ca}}$, $g_{\text{b,K}}$

h_1 , h_2

h

i_{Na}

$i_{\text{Ca,L}}$, $i_{\text{Ca,T}}$

i_{to} , i_{sus}

$i_{\text{K,r}}$, $i_{\text{K,s}}$

i_{K}

i_{f}

$i_{\text{f,Na}}$, $i_{\text{f,K}}$

$i_{\text{b,Na}}$, $i_{\text{b,Ca}}$, $i_{\text{b,K}}$

i_{NaCa}

i_{p}

\bar{i}_{p}

i_{tot}

$i_{\text{tot}}^{\text{a}}(x)$, $i_{\text{tot}}^{\text{s}}(x)$

i_{st}

$i_{\text{K,ACh}}$

$i_{\text{K,ATP}}$

k_{NaCa}

$K_{\text{m,Na}}$, $K_{\text{m,K}}$

one-dimensional model of the intact SA node

Reversal potential for $i_{\text{K,s}}$

Equilibrium potentials for Na^+ , Ca^{2+} , and K^+

Reversal potentials for $i_{\text{Ca,L}}$ and $i_{\text{Ca,T}}$

Faraday's constant

Fraction of activation of $i_{\text{K,r}}$ that occurs slowly

Fraction of inactivation of i_{Na} that occurs slowly

Inactivation variables for $i_{\text{Ca,L}}$ and $i_{\text{Ca,T}}$

Conductance of a current in peripheral or central SA node cell models

Conductance of a current in atrial muscle cell or SA node cell in one-dimensional model of intact SA node at distance x from center of SA node

Conductance of i_{Na}

Conductance of $i_{\text{Ca,L}}$ and $i_{\text{Ca,T}}$

Conductance of i_{to} and i_{sus}

Conductance of $i_{\text{K,r}}$ and $i_{\text{K,s}}$

Conductance of Na^+ and K^+ components of i_{f}

Conductance of $i_{\text{b,Na}}$, $i_{\text{b,Ca}}$, and $i_{\text{b,K}}$

Fast and slow inactivation variables for i_{Na}

Net fractional availability of i_{Na}

TTX-sensitive Na^+ current

L- and T-type Ca^{2+} currents

Transient and sustained components of 4-AP-sensitive current

Rapid and slow delayed rectifying K^+ currents

Sum of $i_{\text{K,r}}$ and $i_{\text{K,s}}$

Hyperpolarization-activated current

Na^+ and K^+ components of i_{f}

Background Na^+ , Ca^{2+} , and K^+ currents

$\text{Na}^+/\text{Ca}^{2+}$ exchanger current

Na^+/K^+ pump current

Maximum i_{p}

Total ionic current in a cell

Total ionic current in atrial muscle cell or SA node cell in one-dimensional model of intact SA node at distance x from center of SA node

Sustained current

ACh-activated K^+ current

ATP-sensitive K^+ current

Scaling factor for i_{NaCa}

Dissociation constants for Na^+ and K^+ activation of i_{p}

| | |
|----------------------------------|--|
| L | Length of string of SA node and atrial tissue in one-dimensional model of intact SA node |
| L^s | Length of string of SA node tissue in one-dimensional model of intact SA node |
| m | Activation variable for i_{Na} |
| MDP | Maximum diastolic potential |
| n_∞ | Steady-state value of n |
| p_a | General activation variable for $i_{K,r}$ |
| $p_{a,f}, p_{a,s}$ | Fast and slow activation variables for $i_{K,r}$ |
| p_i | Inactivation variable for $i_{K,r}$ |
| Q_{10} | Fractional change in a variable with a 10°C increase in temperature |
| r | Activation variable for i_{to} |
| R | Universal gas constant |
| q | Inactivation variable for i_{to} |
| SA node, SAN | Sinoatrial node |
| t | Time |
| T | Absolute temperature |
| TOP | Takeoff potential |
| V | Membrane potential |
| V^a, V^s | Membrane potential of atrial muscle cell or SA node cell in one-dimensional model of intact SA node |
| $V^a(x), V^s(x)$ | Membrane potential of atrial muscle cell or SA node cell in one-dimensional model of intact SA node at distance x from center of SA node |
| x | Distance from center of SA node in one-dimensional model of intact SA node |
| x_s | Activation variable for $i_{K,s}$ |
| y | Activation variable of i_f |
| z | Valency of ion |
| $[Na^+]_i, [Ca^{2+}]_i, [K^+]_i$ | Intracellular Na^+ , Ca^{2+} , and K^+ concentrations |
| $[Na^+]_o, [Ca^{2+}]_o, [K^+]_o$ | Extracellular Na^+ , Ca^{2+} , and K^+ concentrations |
| α_n | Voltage-dependent opening rate constant of n |
| β_n | Voltage-dependent closing rate constant of n |
| γ_{NaCa} | Position of Eyring rate theory energy barrier controlling voltage dependence of i_{NaCa} |
| τ_n | Time constant of n |
| λ | Space constant |

MODEL DEVELOPMENT

Mathematical models of the action potential in peripheral and central cells of the rabbit SA node at 37°C were developed using experimental data from rabbit SA node preparations. New formulations for a number of ionic currents were developed on the basis of newly published data from rabbit

Table 1. *General equations*

$$i_{tot} = i_{Na} + i_{Ca,L} + i_{Ca,T} + i_{to} + i_{sus} + i_{K,r} + i_{K,s} + i_f + i_{b,Na} + i_{b,Ca} + i_{b,K} + i_{NaCa} + i_p \quad (1)$$

$$\frac{dV}{dt} = -\frac{1}{C_m} i_{tot} \quad (2)$$

$$E_{Na} = \frac{RT}{zF} \ln \left(\frac{[Na^+]_o}{[Na^+]_i} \right) \quad (3)$$

$$E_{Ca} = \frac{RT}{zF} \ln \left(\frac{[Ca^{2+}]_o}{[Ca^{2+}]_i} \right) \quad (4)$$

$$E_K = \frac{RT}{zF} \ln \left(\frac{[K^+]_o}{[K^+]_i} \right) \quad (5)$$

Glossary defines all abbreviations used in equations.

SA node cells: i_{Na} , $i_{Ca,L}$, $i_{Ca,T}$, i_{to} , 4-AP-sensitive sustained outward current (i_{sus}), $i_{K,r}$, $i_{K,s}$, and i_f . Full details are given below. The models also include formulations for background currents ($i_{b,Na}$, $i_{b,Ca}$, and $i_{b,K}$), i_p , and i_{NaCa} ; these formulations are similar to those in other models (13, 17, 25). The membrane potential is calculated using Eq. 2 (Table 1). The *Glossary* defines all abbreviations used. Formulations for ionic currents are shown in Tables 2–9. All parameter values are listed in Table 10. Differences in current densities between the peripheral and central SA node cell models are listed in Table 11. Initial values of variables used to run the models are listed in Table 12.

Table 2. *TTX-sensitive Na^+ current (i_{Na})*

$$i_{Na} = g_{Na} m^3 h [Na^+]_o \frac{F^2}{RT} \frac{e^{(V - E_{Na})F/RT} - 1}{e^{VF/RT} - 1} V \quad (6)$$

$$h = (1 - F_{Na})h_1 + F_{Na}h_2 \quad (7)$$

$$F_{Na} = \frac{9.52 \times 10^{-2} \times e^{-6.3 \times 10^{-2} \times (V + 34.4)}}{1 + 1.66e^{-0.225(V + 63.7)}} + 8.69 \times 10^{-2} \quad (8)$$

$$m_\infty = \left(\frac{1}{1 + e^{-V/5.46}} \right)^{1/3} \quad (9)$$

$$\tau_m = \frac{0.6247 \times 10^{-3}}{0.832e^{-0.335(V + 56.7)} + 0.627e^{0.082(V + 65.01)}} + 4 \times 10^{-5} \quad (10)$$

$$\frac{dm}{dt} = \frac{m_\infty - m}{\tau_m} \quad (11)$$

$$h_{1\infty} = \frac{1}{1 + e^{(V + 66.1)/6.4}} \quad (12)$$

$$h_{2\infty} = h_{1\infty} \quad (13)$$

$$\tau_{h_1} = \frac{3.717 \times 10^{-6} \times e^{-0.2815(V + 17.11)}}{1 + 3.732 \times 10^{-3} \times e^{-0.3426(V + 37.76)}} + 5.977 \times 10^{-4} \quad (14)$$

$$\tau_{h_2} = \frac{3.186 \times 10^{-8} \times e^{-0.6219(V + 18.8)}}{1 + 7.189 \times 10^{-5} \times e^{-0.6683(V + 34.07)}} + 3.556 \times 10^{-3} \quad (15)$$

$$\frac{dh_1}{dt} = \frac{h_{1\infty} - h_1}{\tau_{h_1}} \quad (16)$$

$$\frac{dh_2}{dt} = \frac{h_{2\infty} - h_2}{\tau_{h_2}} \quad (17)$$

Table 3. *L-type* Ca^{2+} current ($i_{Ca,L}$)

$$i_{Ca,L} = g_{Ca,L} \left[f_L d_L + \frac{0.006}{1 + e^{-(V+14.1)/6}} \right] (V - E_{Ca,L}) \quad (18)$$

$$\alpha_{d_L} = -14.19 \frac{(V+35)}{e^{-(V+35)/2.5} - 1} - \frac{42.45V}{e^{-0.208V} - 1} \quad (19)$$

$$\beta_{d_L} = \frac{5.71(V-5)}{e^{0.4(V-5)} - 1} \quad (20)$$

$$\tau_{d_L} = \frac{1}{\alpha_{d_L} + \beta_{d_L}} \quad (21)$$

$$d_{L_\infty} = \frac{1}{1 + e^{-(V+23.1)/6}} \quad (22)$$

$$\frac{dd_L}{dt} = \frac{d_{L_\infty} - d_L}{\tau_{d_L}} \quad (23)$$

$$\alpha_{f_L} = \frac{3.12(V+28)}{e^{(V+28)/4} - 1} \quad (24)$$

$$\beta_{f_L} = \frac{25}{1 + e^{-(V+28)/4}} \quad (25)$$

$$\tau_{f_L} = \frac{1}{\alpha_{f_L} + \beta_{f_L}} \quad (26)$$

$$f_{L_\infty} = \frac{1}{1 + e^{(V+45)/5}} \quad (27)$$

$$\frac{df_L}{dt} = \frac{f_{L_\infty} - f_L}{\tau_{f_L}} \quad (28)$$

Model of i_{Na}

The i_{Na} was thought to be absent in SA node cells, and most previous models of the SA node action potential do not include i_{Na} . However, recent experimental results show that

Table 4. *T-type* Ca^{2+} currents ($i_{Ca,T}$)

$$i_{Ca,T} = g_{Ca,T} d_T f_T (V - E_{Ca,T}) \quad (29)$$

$$\alpha_{d_T} = 1.068 e^{(V+26.3)/30} \quad (30)$$

$$\beta_{d_T} = 1.068 e^{-(V+26.3)/30} \quad (31)$$

$$\tau_{d_T} = \frac{1}{\alpha_{d_T} + \beta_{d_T}} \quad (32)$$

$$d_{T_\infty} = \frac{1}{1 + e^{-(V+37)/6.8}} \quad (33)$$

$$\frac{dd_T}{dt} = \frac{d_{T_\infty} - d_T}{\tau_{d_T}} \quad (34)$$

$$\alpha_{f_T} = 15.3 e^{-(V+71.7)/83.3} \quad (35)$$

$$\beta_{f_T} = 15 e^{(V+71.7)/15.38} \quad (36)$$

$$\tau_{f_T} = \frac{1}{\alpha_{f_T} + \beta_{f_T}} \quad (37)$$

$$f_{T_\infty} = \frac{1}{1 + e^{(V+71)/9}} \quad (38)$$

$$\frac{df_T}{dt} = \frac{f_{T_\infty} - f_T}{\tau_{f_T}} \quad (39)$$

Table 5. *4-AP-sensitive* currents (i_{to} and i_{sus})

$$i_{to} = g_{to} q r (V - E_K) \quad (40)$$

$$q_\infty = \frac{1}{1 + e^{(V+59.37)/13.1}} \quad (41)$$

$$\tau_q = 10.1 \times 10^{-3} + \frac{65.17 \times 10^{-3}}{0.57 \times e^{-0.08(V+49)}} + 0.24 \times 10^{-4} \times e^{0.1(V+50.93)} \quad (42)$$

$$\frac{dq}{dt} = \frac{q_\infty - q}{\tau_q} \quad (43)$$

$$r_\infty = \frac{1}{1 + e^{-(V-10.93)/19.7}} \quad (44)$$

$$\tau_r = 2.98 \times 10^{-3} + \frac{15.59 \times 10^{-3}}{1.037 e^{0.09(V+30.61)} + 0.369 e^{-0.12(V+23.84)}} \quad (45)$$

$$\frac{dr}{dt} = \frac{r_\infty - r}{\tau_r} \quad (46)$$

$$i_{sus} = g_{sus} r (V - E_K) \quad (47)$$

i_{Na} is present and physiologically important (27, 33). Demir et al. (13) introduced i_{Na} in their model of the rabbit SA node action potential; the formulation for i_{Na} was based on the experimental data of Colatsky (11) from rabbit Purkinje fibers. However, on the basis of the formulation for i_{Na} from Demir et al., the time dependence of i_{Na} is different from that seen experimentally in rabbit SA node cells (27). The classic formulation for the Na^+ current assumes that the Na^+ conductance is controlled by m^3h , in which m is the activation variable and h is the inactivation variable (26). Most previous formulations for cardiac i_{Na} have used the same term (17). However, recent voltage-clamp experiments on rabbit SA node cells (27, 43) and other cardiac cells have shown that the time course of recovery from inactivation can be best fitted by

Table 6. *Rapid delayed rectifying* K^+ current ($i_{K,r}$)

$$p_a = (1 - F_{K,r}) p_{a,f} + F_{K,r} p_{a,s} \quad (48)$$

$$i_{K,r} = g_{K,r} p_a p_i (V - E_K) \quad (49)$$

$$p_{a,f_\infty} = \frac{1}{1 + e^{-(V+14.2)/10.6}} \quad (50)$$

$$p_{a,s_\infty} = p_{a,f_\infty} \quad (51)$$

$$\tau_{p_{a,f}} = \frac{1}{37.2 e^{(V-9)/15.9} + 0.96 e^{-(V-9)/22.5}} \quad (52)$$

$$\tau_{p_{a,s}} = \frac{1}{4.2 e^{(V-9)/17} + 0.15 e^{-(V-9)/21.6}} \quad (53)$$

$$\frac{dp_{a,f}}{dt} = \frac{p_{a,f_\infty} - p_{a,f}}{\tau_{p_{a,f}}} \quad (54)$$

$$\frac{dp_{a,s}}{dt} = \frac{p_{a,s_\infty} - p_{a,s}}{\tau_{p_{a,s}}} \quad (55)$$

$$p_{i_\infty} = \frac{1}{1 + e^{(V+18.6)/10.1}} \quad (56)$$

$$\tau_{p_i} = 0.002 \quad (57)$$

$$\frac{dp_i}{dt} = \frac{p_{i_\infty} - p_i}{\tau_{p_i}} \quad (58)$$

Table 7. *Slow delayed rectifying K^+ current ($i_{K,s}$)*

$$i_{K,s} = g_{K,s} x_s^2 (V - E_{K,s}) \quad (59)$$

$$E_{K,s} = \frac{RT}{F} \ln \left(\frac{[K^+]_o + 0.12[Na^+]_o}{[K^+]_i + 0.12[Na^+]_i} \right) \quad (60)$$

$$\alpha_{x_s} = \frac{14}{1 + e^{-(V-40)/9}} \quad (61)$$

$$\beta_{x_s} = e^{-V/45} \quad (62)$$

$$x_{s\infty} = \frac{\alpha_{x_s}}{\alpha_{x_s} + \beta_{x_s}} \quad (63)$$

$$\tau_{x_s} = \frac{1}{\alpha_{x_s} + \beta_{x_s}} \quad (64)$$

$$\frac{dx_s}{dt} = \frac{x_{s\infty} - x_s}{\tau_{x_s}} \quad (65)$$

two exponentials; therefore, there are two components of inactivation; hence, two inactivation variables are needed. In the present formulation, three variables are used to govern the kinetics of i_{Na} : m and h_1 and h_2 , a fast and a slow inactivation variable. The equations for i_{Na} are listed in Table 2.

Activation and inactivation curves. Activation curves (corresponding to the steady-state value of m^3) are shown in Fig. 1A. The filled squares show the activation curve based on data from Baruscotti et al. (2) from young rabbit SA node cells at room temperature, and the filled triangles represent data from Muramatsu et al. (43) from cultured rabbit SA node cells at 22–24°C (fits to the experimental data rather than the original data are shown). The solid line is the model-generated activation curve, which fits well with the data of Baruscotti et al. The dashed line is the activation curve from a model of a rabbit atrial cell (41). The general inactivation variable h is the weighted sum of h_1 and h_2 (Eq. 7, Table 2). F_{Na} is the fraction of inactivation that occurs slowly and is dependent on the membrane potential; h_1 and h_2 change with different time constants but have the same steady-state value. Inactivation curves (corresponding to the steady-state value of h) are also shown in Fig. 1A. The open squares show the inactivation curve based on data from Baruscotti et al. from young rabbit SA node cells, and the open triangles represent data from Muramatsu et al. from cultured rabbit SA node cells (fits to the experimental data

Table 9. *Background, pump, and exchanger currents*

$$i_{b,Na} = g_{b,Na} (V - E_{Na}) \quad (74)$$

$$i_{b,K} = g_{b,K} (V - E_K) \quad (75)$$

$$i_{b,Ca} = g_{b,Ca} (V - E_{Ca}) \quad (76)$$

$$i_{NaCa} = k_{NaCa} \frac{[Na^+]_i^3 [Ca^{2+}]_o e^{0.03743V_{NaCa}} - [Na^+]_o^3 [Ca^{2+}]_i e^{0.0374V_{NaCa} - 1}}{1 + d_{NaCa} ([Ca^{2+}]_i [Na^+]_o^3 + [Ca^{2+}]_o [Na^+]_i^3)} \quad (77)$$

$$i_p = i_p^- \left(\frac{[Na^+]_i}{K_{m,Na} + [Na^+]_i} \right) \left(\frac{[K^+]_o}{K_{m,K} + [K^+]_o} \right)^2 \frac{1.6}{1.5 + e^{-(V+60)/40}} \quad (78)$$

rather than the original data are shown). There is a substantial difference between the data from the two groups. It is known that ion channels can change in culture, and this perhaps explains the difference. The model-generated inactivation curve (solid line) is closer to the data of Baruscotti et al. from young rabbit SA node cells. The dashed line is the inactivation curve from the model of a rabbit atrial cell (41).

Kinetics. Because of the rapid activation of i_{Na} , study of i_{Na} activation is difficult, and there are no data from rabbit SA node cells on the time constant of activation (τ_m). Data from the study of Brown et al. (8) on rat ventricular cells were used. Inasmuch as the experiments of Brown et al. were carried out at room temperature (22°C), a Q_{10} of 1.7 (41) was used to correct the data for 37°C. The τ_m is plotted as a function of membrane potential in Fig. 1B, in which the circles show the temperature-corrected experimental data, and the solid line was generated by the model. In Fig. 1C, the time constant of fast inactivation (τ_{h1}) is plotted as a function of membrane potential. The formulation for τ_{h1} was based on data from Muramatsu et al. (43) from cultured rabbit SA node cells (circles in Fig. 1C), Honjo et al. (27) from rabbit SA node cells (triangles), and Brown et al. from rat ventricular cells (squares). A Q_{10} of 1.7 (41) was used to correct the experimental data (collected at 22°C) for 37°C (the temperature-corrected data are shown in Fig. 1C). In Fig. 1C, the solid line was generated by the model and the dashed line is from the model of a rabbit atrial cell (41). In Fig. 1D, the time constant of slow inactivation (τ_{h2}) is plotted as a function of membrane potential. The formulation for τ_{h2} was based on data from Muramatsu et al. from cultured rabbit SA node cells (circles in Fig. 1D) and Brown et al. from rat ventricular cells (squares). A Q_{10} of 1.7 (41) was used to correct the experimental data (collected at 22°C) for 37°C (the temperature-corrected data are shown in Fig. 1D). In Fig. 1D, the solid line was generated by the model and the dashed line is from the model of a rabbit atrial cell (41). In Fig. 1E, the fraction of slow inactivation (F_{Na}) is plotted as a function of membrane potential. The formulation for F_{Na} was based on data from Muramatsu et al. from cultured rabbit SA node cells. In Fig. 1E, the circles show experimental data, and the solid line was generated by the model. Over a wide range of membrane potentials, F_{Na} is ~10% of total inactivation of i_{Na} . Inasmuch as the density of i_{Na} is large in a peripheral SA node cell, ~10% of i_{Na} that inactivates slowly will contribute a substantial inward current during the early period of the action potential.

Simulated current. Figure 1F shows simulated i_{Na} from the peripheral SA node cell model during depolarizing voltage-clamp pulses as well as the current-voltage relationship of i_{Na} from the model (solid line and filled squares). The open circles show the experimental data of Honjo et al. (27) from a rabbit SA node cell with a C_m of 54.5 pF.

Table 8. *Hyperpolarization-activated current (i_f)*

$$i_f = i_{f,Na} + i_{f,K} \quad (66)$$

$$i_{f,Na} = g_{f,Na} y (V - E_{Na}) \quad (67)$$

$$i_{f,K} = g_{f,K} y (V - E_K) \quad (68)$$

$$\alpha_y = e^{-(V+78.91)/26.62} \quad (69)$$

$$\beta_y = e^{(V+75.13)/21.25} \quad (70)$$

$$y_{\infty} = \frac{\alpha_y}{\alpha_y + \beta_y} \quad (71)$$

$$\tau_y = \frac{1}{\alpha_y + \beta_y} \quad (72)$$

$$\frac{dy}{dt} = \frac{y_{\infty} - y}{\tau_y} \quad (73)$$

Table 10. *Parameter values*

| | Peripheral SA Node Cell Model | | Central SA Node Cell Model | | Ratio* |
|-----------------|--------------------------------|----------------------------------|---------------------------------|----------------------------------|----------|
| | Absolute value | Normalized value | Absolute value | Normalized value | |
| C_m | 65 pF | | 20 pF | | |
| d_{NaCa} | 0.0001 | | 0.0001 | | |
| $E_{Ca,L}$ | 46.4 mV | | 46.4 mV | | |
| $E_{Ca,T}$ | 45 mV | | 45 mV | | |
| g_{Na} | 1.2×10^{-6} μ S | 1.85×10^{-8} μ S/pF | 0 S | 0 μ S/pF | ∞ |
| $g_{Ca,L}$ | 6.59×10^{-2} μ S | 1.0×10^{-3} μ S/pF | 0.58×10^{-2} μ S | 2.90×10^{-4} μ S/pF | 3.45 |
| $g_{Ca,T}$ | 1.39×10^{-2} μ S | 2.14×10^{-4} μ S/pF | 0.43×10^{-2} μ S | 2.14×10^{-4} μ S/pF | 1 |
| g_{to} | 36.49×10^{-3} μ S | 5.6×10^{-4} μ S/pF | 4.91×10^{-3} μ S | 2.5×10^{-4} μ S/pF | 2.33 |
| g_{sus} | 1.14×10^{-2} μ S | 1.8×10^{-4} μ S/pF | 6.65×10^{-5} μ S | 3.3×10^{-6} μ S/pF | 54.55 |
| $g_{K,r}$ | 1.60×10^{-2} μ S | 2.46×10^{-4} μ S/pF | 7.97×10^{-4} μ S | 3.99×10^{-5} μ S/pF | 6.17 |
| $g_{K,s}$ | 1.04×10^{-2} μ S | 1.6×10^{-4} μ S/pF | 5.18×10^{-4} μ S | 2.59×10^{-5} μ S/pF | 6.17 |
| $g_{f,Na}$ | 0.69×10^{-2} μ S | 1.05×10^{-4} μ S/pF | 0.0548×10^{-2} μ S | 0.27×10^{-4} μ S/pF | 3.93 |
| $g_{f,K}$ | 0.69×10^{-2} μ S | 1.05×10^{-4} μ S/pF | 0.0548×10^{-2} μ S | 0.27×10^{-4} μ S/pF | 3.93 |
| $g_{b,Na}$ | 1.89×10^{-4} μ S | 2.9×10^{-6} μ S/pF | 5.8×10^{-5} μ S | 2.91×10^{-6} μ S/pF | 1 |
| $g_{b,Ca}$ | 4.3×10^{-5} μ S | 6.61×10^{-7} μ S/pF | 1.32×10^{-5} μ S | 6.62×10^{-7} μ S/pF | 1 |
| $g_{b,K}$ | 8.19×10^{-5} μ S | 1.3×10^{-6} μ S/pF | 2.52×10^{-5} μ S | 1.3×10^{-6} μ S/pF | 1 |
| i_p | 0.16 nA | 2.46×10^{-3} nA | 4.78×10^{-2} nA | 2.46×10^{-3} nA | 1 |
| k_{NaCa} | 0.88×10^{-5} nA | 1.36×10^{-7} nA | 0.27×10^{-5} nA | 1.36×10^{-7} nA | 1 |
| $[Na^+]_o$ | 140 mM | | 140 mM | | |
| $[Na^+]_i$ | 8 mM | | 8 mM | | |
| $[Ca^{2+}]_o$ | 2 mM | | 2 mM | | |
| $[Ca^{2+}]_i$ | 0.0001 mM | | 0.0001 mM | | |
| $[K^+]_o$ | 5.4 mM | | 5.4 mM | | |
| $[K^+]_i$ | 140 mM | | 140 mM | | |
| $K_{m,K}$ | 0.621 | | 0.621 | | |
| $K_{m,Na}$ | 5.64 | | 5.64 | | |
| γ_{NaCa} | 0.5 | | 0.5 | | |

* Ratio of normalized conductance or current in peripheral to central SA node cell model.

Models of $i_{Ca,L}$ and $i_{Ca,T}$

The equations for $i_{Ca,L}$ are listed in Table 3. Activation and inactivation curves [corresponding to the steady-state values of the activation variable (d_L) and the inactivation variable (f_L)] are shown in Fig. 2A. The squares and circles show data from Hagiwara et al. (22) and Fermini and Nathan (19), respectively, from rabbit SA node cells at 36–37°C, and the solid lines were generated by the model. For the time constants of activation and inactivation, we followed Demir et al. (13) and used the data of Nilius (46) from guinea pig SA node cells after temperature correction (from 25 to 37°C with a Q_{10} of 2.3). Figure 2C shows simulated $i_{Ca,L}$ from the peripheral

SA node cell model during depolarizing voltage-clamp pulses. Figure 2D shows current-voltage relationships for $i_{Ca,L}$ (circles); the open circles show data from Hagiwara et al. from a rabbit SA node cell, and the filled circles (and solid line) show data from the peripheral SA node cell model.

The equations for $i_{Ca,T}$ are listed in Table 4. Activation and inactivation curves [corresponding to the steady-state values of the activation variable (d_T) and the inactivation variable (f_T)] are shown in Fig. 2B. The squares, circles, and triangles show data from Hagiwara et al. (22), Fermini and Nathan (19), and Lei et al. (38), respectively, from rabbit SA node cells at ~37°C. In the model the activation and inactivation curves (solid lines) were computed using equations (Eqs. 33 and 38, Table 4) formulated by Lei (35) and Lei et al. (38) based on their experimental data from rabbit SA node cells at

Table 11. *Current densities in the SA node cell models*

| | Current Density, pA/pF | | Ratio* | Potential, mV |
|------------|------------------------|--------|----------|---------------|
| | Periphery | Center | | |
| i_{Na} | 78 | 0 | ∞ | -10 |
| $i_{Ca,L}$ | 11.15 | 3.23 | 3.45 | 0 |
| $i_{Ca,T}$ | 5.60 | 5.60 | 1 | -10 |
| i_{to} | 36.0 | 15.45 | 2.33 | +50 |
| i_{sus} | 29.45 | 0.54 | 54.55 | +50 |
| $i_{K,r}$ | 5.97 | 0.97 | 6.17 | -10 |
| $i_{K,s}$ | 4.08 | 0.66 | 6.17 | +40 |
| i_f | 13.2 | 3.36 | 3.97 | -110 |
| $i_{b,Na}$ | 0.43 | 0.43 | 1 | -100 |
| $i_{b,K}$ | 0.002 | 0.002 | 1 | -100 |
| $i_{b,Ca}$ | 0.13 | 0.13 | 1 | -100 |
| i_{NaCa} | 0.013 | 0.013 | 1 | -100 |
| i_p | 0.098 | 0.098 | 1 | -100 |

* Ratio of current densities in peripheral to central SA node cell model.

Table 12. *Initial values*

| | Peripheral SA Node Cell Model | Central SA Node Cell Model |
|-----------|-------------------------------|----------------------------|
| V, mV | -64.35 | -51.44 |
| m | 0.124 | |
| h_1 | 0.595 | |
| h_2 | 5.250×10^{-2} | |
| d_L | 8.450×10^{-2} | 5.912×10^{-2} |
| f_L | 0.987 | 0.825 |
| d_T | 1.725×10^{-2} | 0.106 |
| f_T | 0.436 | 0.119 |
| y | 5.280×10^{-2} | 3.775×10^{-2} |
| r | 1.970×10^{-2} | 3.924×10^{-2} |
| q | 0.663 | 0.358 |
| n | 7.670×10^{-2} | 5.700×10^{-2} |
| $p_{a,f}$ | 0.400 | 0.470 |
| $p_{a,s}$ | 0.327 | 0.637 |
| p_i | 0.991 | 0.965 |

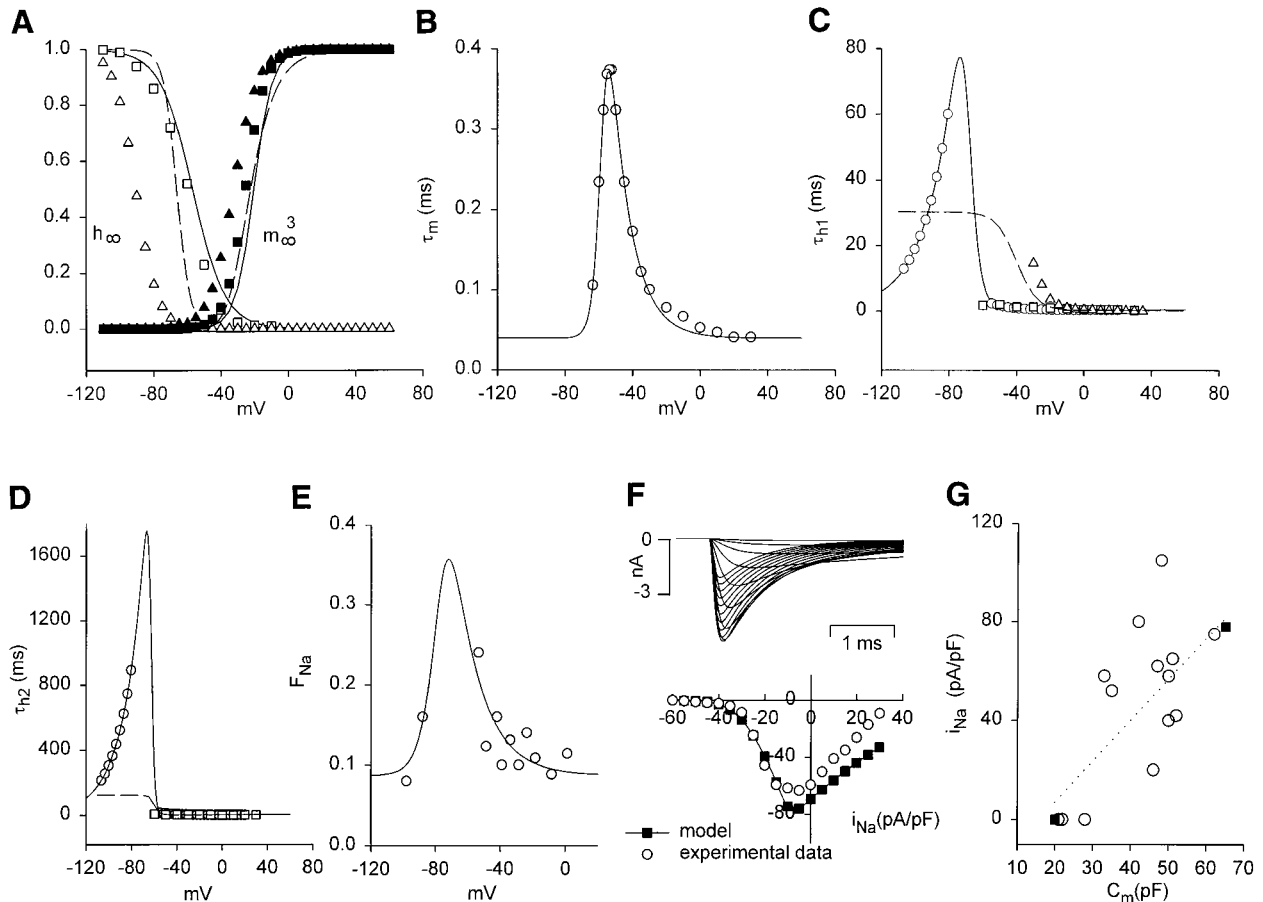


Fig. 1. TTX-sensitive Na^+ current (i_{Na}). **A**: activation (m_{∞}^3 , filled symbols) and inactivation (h_{∞} , open symbols) curves. **B**: time constant of activation (τ_m). **C**: time constant of fast inactivation (τ_{h1}). **D**: time constant of slow inactivation (τ_{h2}). **E**: fraction of i_{Na} inactivation that occurs slowly (F_{Na}). **F**: simulated i_{Na} during 10-ms voltage-clamp pulses to -55 to $+40$ mV (in 5-mV increments) from a holding potential of -60 mV (top) and current-voltage relationships for i_{Na} (bottom). For the current-voltage relationships, i_{Na} was measured as peak inward current. **G**: density of i_{Na} (measured from the peak inward current during a pulse to -5 mV) plotted against cell capacitance (C_m). \circ , Data from Honjo et al. (27) from rabbit sinoatrial (SA) node cells; dotted line, regression line; \blacksquare , values used in the peripheral ($C_m = 65$ pF) and central ($C_m = 20$ pF) SA node cell models.

37°C . In the model we used equations (Eqs. 30–32 and 35–37, Table 4) formulated by Hagiwara et al. (22) for the time constants of activation and inactivation (τ_{dT} and τ_{iT}) in rabbit SA node cells. Figure 2C shows simulated $i_{\text{Ca,T}}$ during depolarizing voltage-clamp pulses. Figure 2D shows current-voltage relationships for $i_{\text{Ca,T}}$ (squares); the open squares show data from Hagiwara et al. from a rabbit SA node cell, and the filled squares (and solid line) show data from the peripheral SA node cell model.

Model of 4-AP-Sensitive Current

Previous models of the SA node action potential did not incorporate i_{to} . However, i_{to} is now known to be present in the rabbit SA node and to play an important role (6, 28, 39). The i_{to} is known to be blocked by 4-AP. In rabbit SA node cells, 4-AP blocks a transient outward current as well as a sustained outward current. It is unclear whether the transient and sustained components represent two phases of one current or two separate currents (28). We chose to treat the two components as separate mathematical entities: i_{to} and i_{sus} . Honjo et al. (28) found no difference in the activation curves for i_{to} and i_{sus} , and therefore in the model we used the same activation variable (r) for i_{to} and i_{sus} . Of course, the inacti-

vation variable (q) only governs i_{to} . The equations for i_{to} and i_{sus} are listed in Table 5.

Activation and inactivation curves. Activation curves (corresponding to the steady-state value of the activation variable, r) are shown in Fig. 3A. The filled triangles, filled squares, and filled diamonds show data from Honjo et al. (28) from rabbit SA node cells with capacitances of 63.4, 34.5, and 20.3 pF at 25°C ; the activation curves are for the sum of i_{to} and i_{sus} . The filled hexagons show data from Lei et al. (39) from rabbit SA node cells at 35°C ; the activation curve is for i_{to} only. The filled circles show data from Giles and van Ginneken (21) from rabbit crista terminalis cells at $\sim 20.5^\circ\text{C}$; because of the method used, the activation curve is for the sum of i_{to} and i_{sus} (if the latter was present). The solid line shows the activation curve generated by the model. Inactivation curves for i_{to} only (corresponding to the steady-state value of q) are also shown in Fig. 3A. Inactivation curves are shown from Honjo et al. (28) from rabbit SA node cells (open triangles, open squares, open diamonds: data from cells with capacitances of 63.4, 47.1, and 23.6 pF, respectively), Lei et al. from rabbit SA node cells (open hexagons), Giles and van Ginneken from rabbit crista terminalis cells (open circles), and the present model (solid line). The model-generated

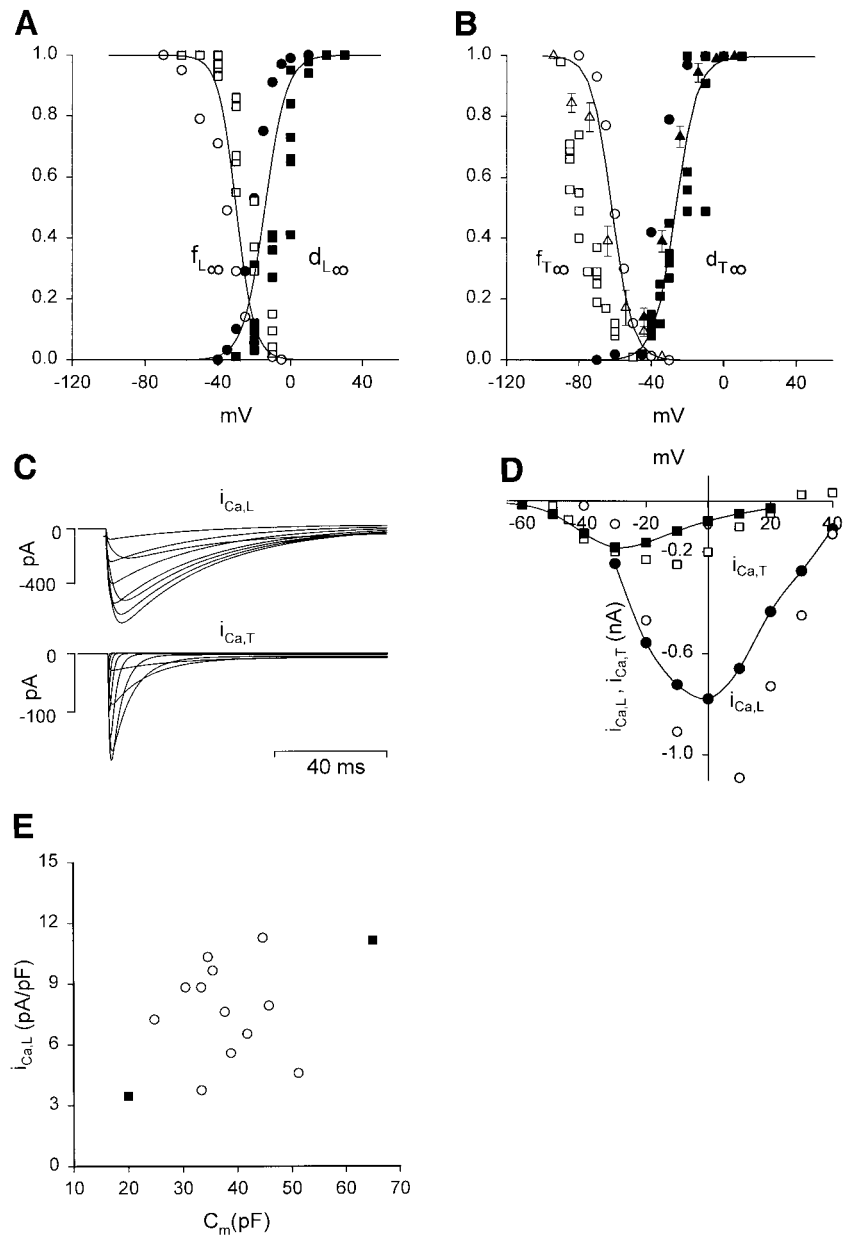


Fig. 2. L- and T-type Ca^{2+} currents ($i_{\text{Ca,L}}$ and $i_{\text{Ca,T}}$). **A**: activation ($d_{L\infty}$, filled symbols) and inactivation ($f_{L\infty}$, open symbols) curves for $i_{\text{Ca,L}}$. **B**: activation ($d_{T\infty}$, filled symbols) and inactivation ($f_{T\infty}$, open symbols) curves for $i_{\text{Ca,T}}$; error bars, SE. **C**: simulated $i_{\text{Ca,L}}$ (300-ms voltage-clamp pulses to -30 to $+40$ mV in 10-mV increments from a holding potential of -40 mV) and $i_{\text{Ca,T}}$ (300-ms voltage-clamp pulses to -70 to $+10$ mV in 10-mV increments from a holding potential of -80 mV). **D**: current-voltage relationships for $i_{\text{Ca,L}}$ (circles) and $i_{\text{Ca,T}}$ (squares); $i_{\text{Ca,L}}$ and $i_{\text{Ca,T}}$ were measured as peak inward current. **E**: density of $i_{\text{Ca,L}}$ (measured from the peak inward current during a pulse to 0 mV) plotted against C_m . \circ , Data from Honjo et al. (27) from rabbit SA node cells; \blacksquare , values used in the peripheral ($C_m = 65$ pF) and central ($C_m = 20$ pF) SA node cell models.

inactivation curve is close to the data of Lei et al. from rabbit SA node cells at 35°C .

Kinetics. The time constant of activation of i_{to} and i_{sus} (τ_r) is shown in Fig. 3B. The circles show data from Giles and van Ginneken (21) from rabbit crista terminalis cells. Inasmuch as the experimental data were collected at 24°C , a Q_{10} of 2.18 (41) was used to correct the data for 37°C (the temperature-corrected data are shown in Fig. 3B). The solid line was generated by the model. Figure 3C shows the time constant of inactivation of i_{to} (τ_q). The squares and triangles show data from Honjo et al. (28) from rabbit SA node cells for the fast and slow components of inactivation [data collected at 25°C corrected for 37°C with a Q_{10} of 2.18 (41)]. The circles show data from Giles and van Ginneken from rabbit crista terminalis cells [data collected at $\sim 20.5^\circ\text{C}$ corrected for 37°C with a Q_{10} of 2.18 (41)]. The solid line was generated by the model.

Simulated current. Figure 3D shows simulated 4-AP-sensitive current ($i_{\text{to}} + i_{\text{sus}}$) from the peripheral SA node cell model during depolarizing voltage-clamp pulses. The cur-

rents are similar to 4-AP-sensitive currents in rabbit SA node cells (28, 39). Current-voltage relationships for i_{to} are shown in Fig. 3E. The open circles show data from Lei et al. (39) from rabbit SA node cells, and the filled circles (and solid line) show data from the peripheral SA node cell model.

Model of $i_{\text{K,r}}$

Recent experiments have shown that i_{K} in rabbit SA node cells (29, 37, 51) can be separated into two kinetically different components, $i_{\text{K,r}}$ and $i_{\text{K,s}}$. A formulation for the delayed rectifying K^+ current with two components, $i_{\text{K,r}}$ and $i_{\text{K,s}}$, was constructed; the equations are listed in Tables 6 and 7. Equations for $i_{\text{K,r}}$ take the general form suggested by Shibasaki (56) with an activation variable (p_a) and inactivation variable (p_i).

Activation and inactivation curves. Activation and deactivation of $i_{\text{K,r}}$ in rabbit SA node cells have double-exponential time courses (37, 51). To model this, we have used two

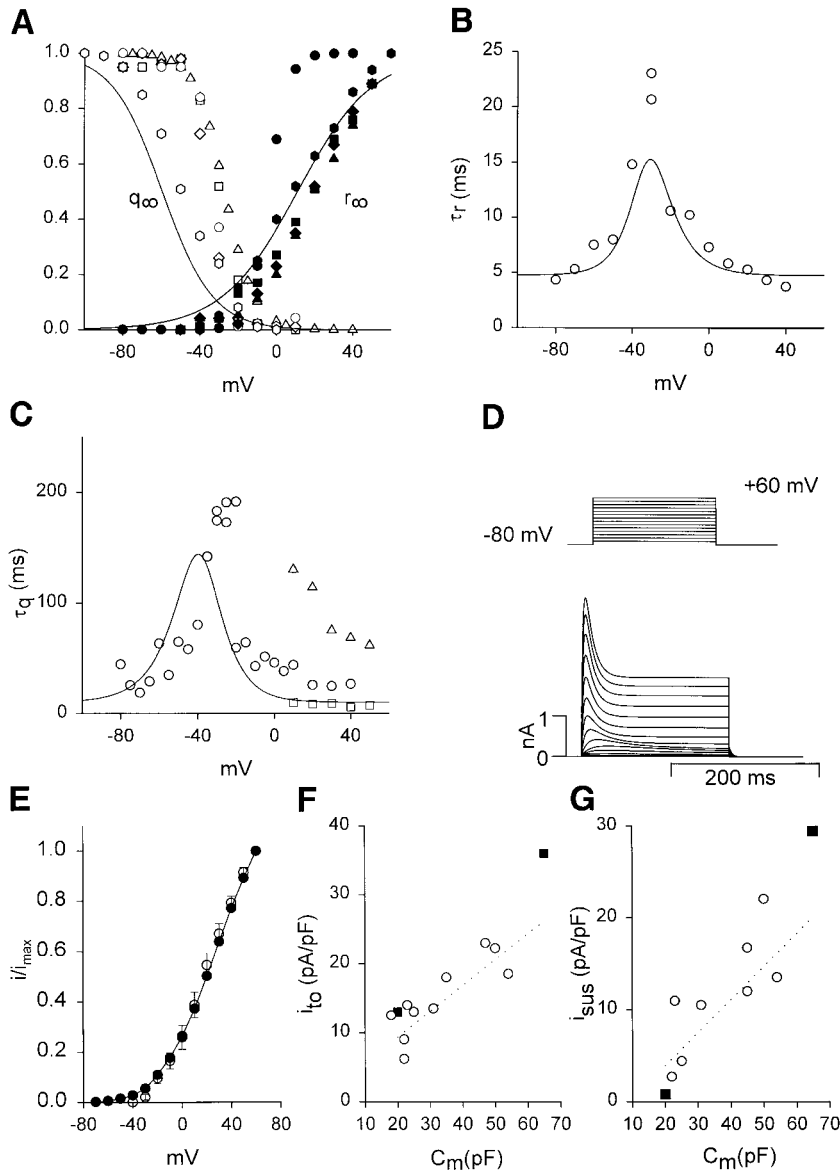


Fig. 3. Transient and sustained components of 4-aminopyridine (4-AP)-sensitive currents (i_{to} and i_{sus}). A: activation (r_{∞} , filled symbols) and inactivation (q_{∞} , open symbols) curves. B: time constant of activation (τ_a). C: time constant of inactivation (τ_q). D: simulated 4-AP-sensitive current during 200-ms voltage-clamp pulses to -70 to +60 mV (in 10-mV increments) from a holding potential of -80 mV (top, voltage-clamp protocol; bottom, current). E: current-voltage relationship for i_{to} (measured as peak outward current at the start of the pulse and the current at the end of the pulse; currents have been normalized to the maximum current at +60 mV); error bars, SE. F and G: densities of i_{to} (F, measured as the difference between the peak 4-AP-sensitive outward current during a 200-ms pulse to +50 mV from a holding potential of -80 mV and the current at the end of the pulse) and i_{sus} (G, measured as the 4-AP-sensitive current at the end of a 200-ms pulse to +50 mV from a holding potential of -80 mV) plotted against C_m . \circ , Data from Lei et al. (39) from rabbit SA node cells; dotted lines, regression lines; \blacksquare , values used in the peripheral ($C_m = 65$ pF) and central ($C_m = 20$ pF) SA node cell models.

activation variables: a fast activation variable ($p_{a,f}$) and a slow activation variable ($p_{a,s}$). The general activation variable (p_a) is the weighted sum of the fast and slow activation variables (Eq. 48, Table 6). In rabbit SA node cells, experimental data have shown no distinct dependence of the fraction of inactivation that occurs slowly ($F_{K,r}$) on membrane potential, and the ratio of the slow to the fast component of activation of $i_{K,r}$ is 2:3 (37). In the model, $F_{K,r}$ is assumed to be constant with a value of 0.4. Figure 4A shows activation curves corresponding to the steady-state value of p_a (we assume that $p_{a,f}$ and $p_{a,s}$ are the same and equal to p_a). The triangles represent data from Lei and Brown (37) from rabbit SA node cells at 37°C (fit to the experimental data rather than the original data is shown). The solid line was generated by the present model and is close to the data of Lei and Brown. In a model of a guinea pig ventricular cell, Noble et al. (50) assumed that the steady-state values of $p_{a,f}$ and $p_{a,s}$ are different, and in the right-hand part of Fig. 4A the long dashed and short dashed lines show the dependence of $p_{a,f}$ and $p_{a,s}$, respectively, from the model of Noble et al. on membrane potential.

Inactivation variable. Figure 4A shows inactivation curves (corresponding to the steady-state value of p_i). In the model the inactivation curve (solid line) was computed using an equation (Eq. 56, Table 6) formulated by Ito and Ono (29, 51) based on their data (circles) from rabbit SA node cells at 33°C. The dashed line is from the model of a guinea pig ventricular cell (50). There appears to be a nearly -18-mV shift in the inactivation curve in rabbit SA node cells compared with that in guinea pig ventricular cells.

Kinetics. The time constants of the fast and slow activation variables ($\tau_{p_{a,f}}$ and $\tau_{p_{a,s}}$) are bell-shaped functions of membrane potentials, as shown in Fig. 4, B and C. In the model the time constants (solid lines) were computed using equations (Eqs. 52 and 53, Table 6) formulated by Ono and Ito (51) based on their experimental data (circles) for rabbit SA node cells. The dashed lines in Fig. 4, B and C, show the time constants used for the guinea pig ventricular cell model of Noble et al. (50). It appears that $\tau_{p_{a,f}}$ and $\tau_{p_{a,s}}$ are larger in guinea pig ventricular cells than in rabbit SA node cells. No experimental data are available on the relationship between the time constant of inactivation (τ_{pi}) and potential in the

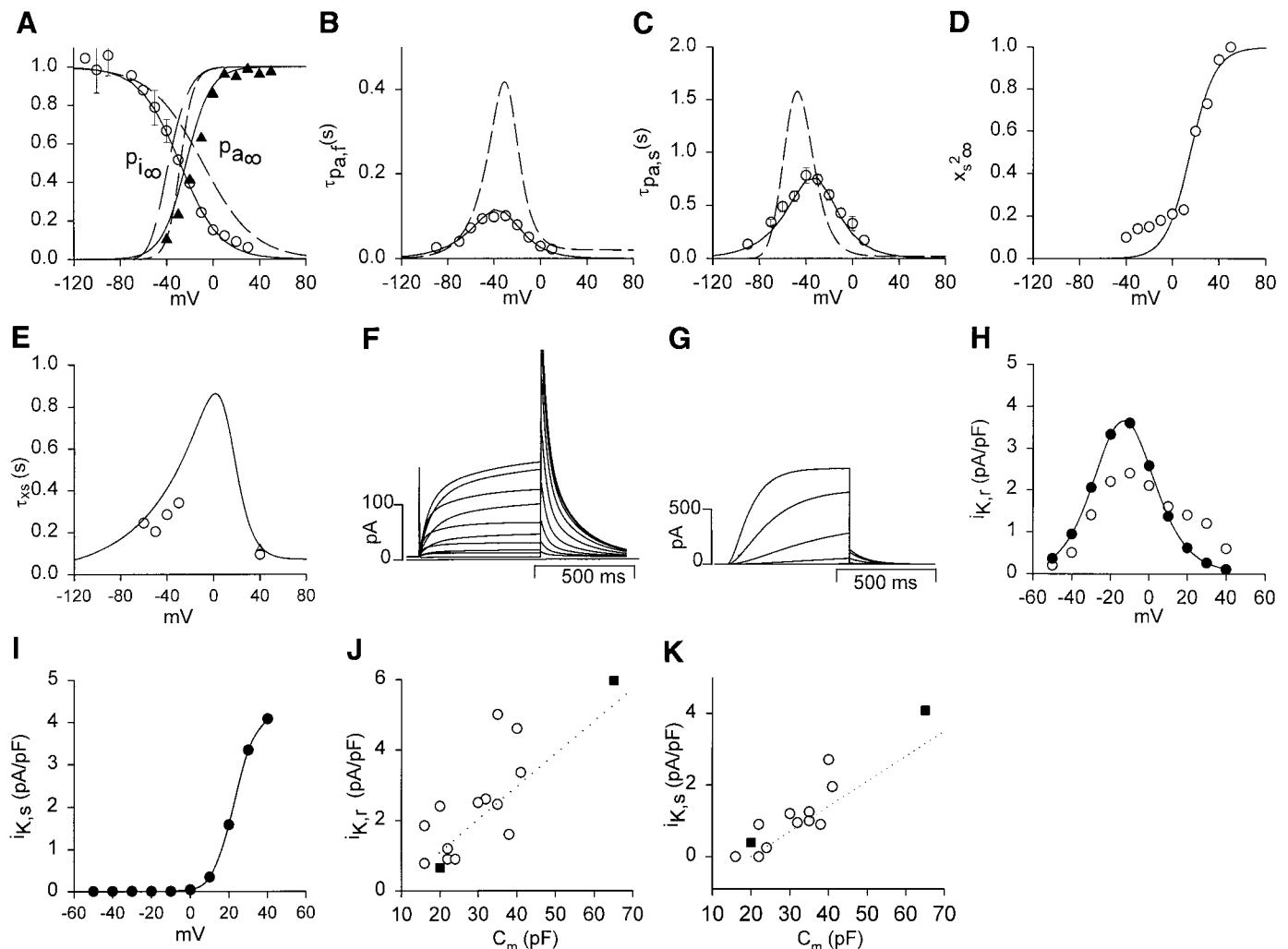


Fig. 4. Rapid and slow delayed rectifying currents ($i_{K,r}$ and $i_{K,s}$). A: activation ($p_{a\infty}$, filled symbols) and inactivation ($p_{i\infty}$, open symbols) curves for $i_{K,r}$; error bars, SE. B: fast time constant of activation of $i_{K,r}$ ($\tau_{pa,r}$). C: slow time constant of activation of $i_{K,r}$ ($\tau_{pa,s}$); error bars, SE. D: activation curve for $i_{K,s}$. E: time constant of activation of $i_{K,s}$. F and G: simulated $i_{K,r}$ (F) and $i_{K,s}$ (G) during 1-s pulses applied to potentials between -50 and +40 mV (in 10-mV increments) from a holding potential of -60 mV. H and I: current-voltage relationships for $i_{K,r}$ (H) and $i_{K,s}$ (I). Currents were measured at the end of the voltage-clamp pulses. J and K: densities of $i_{K,r}$ (J, measured as the peak 3 μ M E-4031-sensitive tail current after a 1-s pulse to -10 mV from a holding potential of -50 mV) and $i_{K,s}$ (K, measured as the peak 3 μ M E-4031-insensitive tail current after a 1-s pulse to +40 mV from a holding potential of -50 mV) plotted against C_m . \circ , Data from M. Lei (unpublished observations) from rabbit SA node cells; dotted lines, regression lines; \blacksquare , values used in the peripheral ($C_m = 65$ pF) and central ($C_m = 20$ pF) SA node cell models.

rabbit SA node. Here we assume that τ_{pi} is independent of the membrane potential and has a fixed value of 0.002 s, as suggested by Ono and Ito.

The $i_{K,r}$ has been consistently observed to reverse direction at the K^+ equilibrium potential (E_K) (51); therefore, only K^+ is assumed to carry $i_{K,r}$, and the reversal potential is equal to E_K .

Simulated current. Figure 4F shows simulated $i_{K,r}$ from the peripheral SA node cell model during depolarizing voltage-clamp pulses. Figure 4H shows the current-voltage relationship of $i_{K,r}$ ($i_{K,r}$ measured at the end of the pulse). The open circles show data from Ito and Ono (29) from rabbit SA node cells, and the filled circles (and solid line) show data from the peripheral SA node cell model. The current-voltage relationship from the model is roughly similar to the experimental data.

Model of $i_{K,s}$

The slow sigmoidal activation of $i_{K,s}$ is modeled by squaring a gating variable (x_s). Figure 4D shows the activation curve (corresponding to the steady-state value of x_s^2). The circles show data from Lei and Brown (37) from rabbit SA node cells at 37°C, and the solid line is the activation curve generated by the model. There are limited experimental data available for the time constant of the activation (τ_{xs}) of $i_{K,s}$ in rabbit SA node cells [triangle in Fig. 4E (37)]. Instead, we used equations (Eqs. 61, 62, and 64, Table 7) formulated by Heath and Terrar (24) based on their data (circles) from guinea pig ventricular cells at 35–36°C, as shown in Fig. 4E; in Fig. 4E the solid line was generated using the model. The $i_{K,s}$ has been observed to reverse at voltages positive to E_K , which suggests that the

$i_{K,s}$ channel is permeable to an ion in addition to K^+ (23). We assumed that $i_{K,s}$ is permeable to a small extent to Na^+ . The reversal potential of $i_{K,s}$ is shown in Table 7. Figure 4*G* shows simulated $i_{K,s}$ from the peripheral SA node cell model during depolarizing voltage-clamp pulses. Figure 4*I* shows a current-voltage relationship for $i_{K,s}$ from the peripheral SA node cell model.

Model of i_f

The i_f is a mixed current and is carried by Na^+ and K^+ . In our formulation, i_f has two components, $i_{f,K}$ and $i_{f,Na}$. The equations are listed in Table 8. Figure 5*A* shows activation curves (corresponding to the steady-state value of y). In Fig. 5*A*, the triangles and squares show data from Liu et al. (42) from rabbit SA node cells at 35–36°C, the circles show data from van Ginneken and Giles (57) from rabbit SA node cells at 30–33°C, and the solid line was generated by the model. Figure 5*B* shows the time constant of activation of i_f (τ_y). In Fig. 5*B*, the triangles and circles show data from Liu et al. and van Ginneken and Giles, respectively, from rabbit SA node cells, and the solid line was generated by the model. Figure 5*C* shows simulated i_f from the peripheral SA node cell model during hyperpolarizing voltage-clamp pulses. Figure 5*D* shows current-voltage relationships for i_f . The open triangles show data from Honjo et al. from a rabbit SA node cell at 36°C with a C_m of 44.7 pF, and the open circles show data from Honjo et al. from a smaller rabbit SA node cell at

36°C with a C_m of 20.2 pF. The filled circles (and solid line) show data from the peripheral SA node cell model ($C_m = 65$ pF), and the filled squares (and solid line) show data from the central SA node cell model ($C_m = 20$ pF). The threshold of i_f in the model is -40 mV, which is in the range of that seen experimentally in rabbit SA node cells (14–16, 57) but more positive than that seen by Honjo et al.

Regional Differences in Ionic Current Densities

The variation in electrical activity from the periphery to the center of the SA node (as described in the introduction) could be the result of a gradual decrease in the electrotonic influence of the surrounding atrial muscle (with more hyperpolarized diastolic potentials) from the periphery to the center. However, experiments using ligated or dissected small pieces of tissue from different regions of the rabbit SA node (in which the large mass of surrounding atrial muscle is removed) also show marked differences in the electrophysiological characteristics of the tissue from the periphery and center of the SA node (33). Immunocytochemical studies have shown that atrial cells are intermingled with SA node cells in the periphery of the SA node in several species (52). It has been conjectured (58) that the electrophysiological properties of pacemaker cells in the SA node are roughly uniform throughout the SA node, and the apparent regional differences in electrical activity in the intact SA node are the result of a progressive decrease in the percentage of intermingling

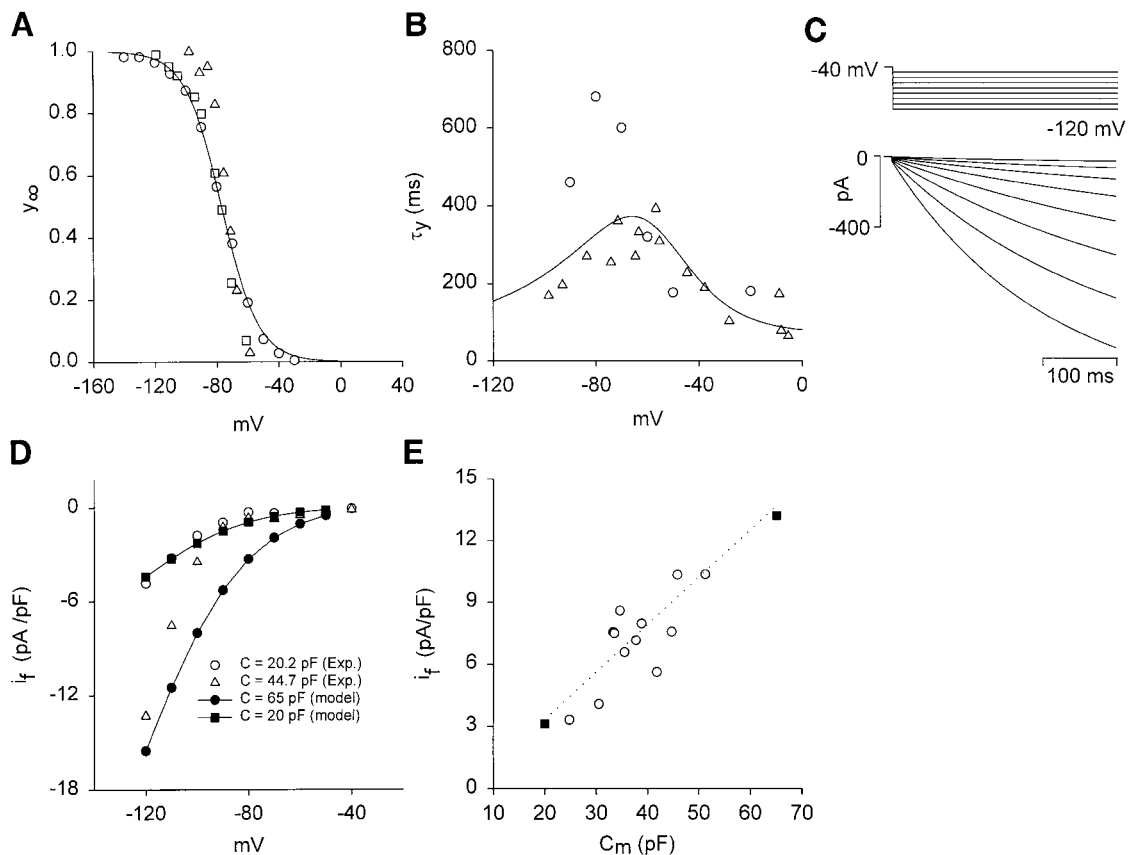


Fig. 5. Hyperpolarization-activated current (i_f). *A*: activation curves. *B*: time constant of activation (τ_y). *C*: simulated i_f during 300-ms pulses to potentials from -50 to -120 mV (in 10-mV increments) from a holding potential of -40 mV (*top*, voltage-clamp protocol; *bottom*, i_f). *D*: current-voltage relationships for i_f ; i_f was measured as the increase in inward current from the beginning to the end of the pulses. *E*: density of i_f (measured during pulse to -110 mV) plotted against C_m . \circ , data from Honjo et al. (27) from rabbit SA node cells; dotted lines, regression lines; \blacksquare , values used in the peripheral ($C_m = 65$ pF) and central ($C_m = 20$ pF) SA node cell models.

atrial cells toward the center, giving rise to a progressive decrease in their hyperpolarizing influence from the periphery toward the center. However, we have little evidence of such intermingling in the rabbit SA node (12). Furthermore, in single SA node cells from the rabbit, we record a range of electrical activities similar to that observed in the different regions of the intact SA node (27). Therefore, we believe that the properties of rabbit SA node cells are not uniform, as suggested by others (58). The size of cells varies from the periphery to the center of the rabbit SA node: cells are large in the periphery and small in the center (in the center, the cells are $<8\ \mu\text{m}$ diameter and $25\text{--}30\ \mu\text{m}$ long) (3). We have shown that the electrical activity of rabbit SA node cells is correlated with cell size (as measured by C_m), and, as expected, large cells have properties characteristic of the periphery of the SA node and small cells have properties characteristic of the center (see the introduction). The densities of a number of ionic currents are dependent on cell size (see the introduction and below). In construction of the models, we assumed that a peripheral cell is large in size, with a C_m of 65 pF, and a central cell is small in size, with a C_m of 20 pF. These values of C_m represent the approximate maximum and minimum values measured experimentally for rabbit SA node cells (27, 28, 36, 39).

Ionic current densities for the peripheral and central SA node cell models are listed in Table 11. For some but not all currents, the relationship between current density and C_m has been determined for rabbit SA node cells, and the final panels of Figs. 1–5 show the densities of various currents plotted against C_m . The open circles are experimental data (27, 28, 39; i_{K_r} and i_{K_s} data from unpublished observations), and the filled squares are the chosen values for the peripheral and central SA node cell models. The experimentally measured densities of i_{Na} , i_{to} , i_{sus} , i_{K_r} , i_{K_s} , and i_f are significantly correlated with C_m and are larger in cells with higher C_m (Figs. 1 and 3–5) (27, 28, 36, 39; i_{K_r} and i_{K_s} data from unpublished observations). Values chosen for the densities of these currents for the peripheral and central SA node cell models are within the experimental range and are greater in the peripheral SA node cell model. Although the density of $i_{Ca,L}$ measured experimentally is not significantly correlated with C_m (27), it was necessary to increase the density of $i_{Ca,L}$ in the peripheral SA node cell model compared with that in the central SA node cell model (Fig. 2E). Despite this, the chosen values for the density of $i_{Ca,L}$ in the peripheral and central SA node cell models are reasonably consistent with the experimental values (Fig. 2E).

During the development of the models, there were no experimental data available on the relationship between the densities of i_{K_r} and i_{K_s} and C_m for rabbit SA node cells. Some data were available: Lei and Brown (37) had reported that the ratio of the amplitude of i_{K_r} to i_{K_s} tails after a 1-s pulse to $+40\ \text{mV}$ from a holding potential of $-40\ \text{mV}$ was $1.0\text{--}0.4$, and, therefore, in the peripheral and central SA node cell models, the ratio was set at $1.0\text{--}0.3$. Although there were no direct measurements of the density of i_{K_r} in rabbit SA node cells with different values of C_m , various indirect lines of evidence suggested that the density of i_{K_r} is greater in peripheral than in central SA node cells. First, although complete block of i_{K_r} by $1\ \mu\text{M}$ E-4031 abolishes pacemaker activity in tissue from the periphery and center of the rabbit SA node, partial block of i_{K_r} by $0.1\ \mu\text{M}$ E-4031 abolishes pacemaker activity in central but not peripheral tissue (32). One explanation for this different response to partial block of i_{K_r} is that the density of i_{K_r} is greater in the periphery of the SA node (32). Second, an immunocytochemical study examined the distribution of ERG (channel protein responsible for

i_{K_r}) in the ferret SA node (7). If the anatomy of the SA node in the ferret is similar to that of the rabbit, the data from the study support the possibility that the density of i_{K_r} is greater in the periphery of the SA node: the labeling of ERG was little in the intercaval region (where the center of the SA node is located in the rabbit at least) and substantial close to the crista terminalis (where the periphery of the SA node is located in the rabbit at least). Finally, in the models of peripheral and central SA node action potentials, it was necessary to increase the density of i_{K_r} in the peripheral cell model compared with that in the central cell model to obtain some of the characteristic differences between the two regions (see Fig. 10). After the development of the models, experimental measurements of the densities of i_{K_r} and i_{K_s} became available (Fig. 4, J and K , open circles) from our laboratory in rabbit SA node cells (unpublished observations). Although the densities of i_{K_r} and i_{K_s} in the peripheral and central SA node models were set before the experimental data became available, they are within the experimental range obtained from rabbit SA node cells.

In the case of currents for which there are no data concerning current density and C_m , the current density was assumed to be the same in peripheral and central SA node cells.

Intracellular Ionic Concentrations

Previous SA node models have included computation of concentrations of intracellular Na^+ and Ca^{2+} (13, 18, 49, 59). In the present models, all intracellular ion concentrations are assumed to be constant (see Table 10 for values). There are various reasons for this: 1) little is known about intracellular Na^+ in the SA node, and there is only one report about intracellular Ca^{2+} in the rabbit SA node (40); 2) nothing is known about differences in intracellular Na^+ and Ca^{2+} handling between the periphery and center of the SA node; 3) intracellular Na^+ changes only slowly over several minutes, and over a few beats intracellular Na^+ is approximately constant; 4) buffering intracellular Ca^{2+} with 1,2-bis(2-aminophenoxy)ethane- N,N,N',N' -tetraacetic acid-AM or reducing the amplitude of the intracellular Ca^{2+} transient with ryanodine does not abolish spontaneous activity in rabbit SA node cells (40), although it can produce a decrease in the rate of spontaneous action potentials (40); and 5) much of our data concerning the dependence of electrical activity and the density of ionic currents on C_m was obtained from rabbit SA node cells in which intracellular Ca^{2+} was buffered with EGTA (27, 28). Because of points 1 and 2, inclusion of intracellular Na^+ and Ca^{2+} handling in the models would be based on speculation to a large degree, and, because of points 3–5, inclusion of intracellular Na^+ and Ca^{2+} handling in the models is not essential for reasonably accurate calculation of electrical activity (over a few beats at least). Inclusion of intracellular Ca^{2+} handling may be important if inward i_{NaCa} triggered by the intracellular Ca^{2+} transient plays a significant role in electrical activity: the slowing of spontaneous activity by 1,2-bis(2-aminophenoxy)ethane- N,N,N',N' -tetraacetic acid-AM or ryanodine could indicate such a role, but even in these cases the slowing may be the result of actions on other currents (40); the role of inward i_{NaCa} triggered by the intracellular Ca^{2+} transient in the SA node is, therefore, unclear. Despite these arguments that the inclusion of intracellular Na^+ and Ca^{2+} handling is not crucial, future models will have to address this shortcoming.

Comparison of the Models of Peripheral and Central SA Node Action Potentials With Action Potentials Measured Experimentally From the Rabbit SA Node

After construction of the models as described above, the configuration of the simulated action potentials was compared with the configuration of action potentials measured experimentally from rabbit SA node cells (with different values of C_m) at 35°C (27) and from small balls of tissue from the periphery and center of the rabbit SA node at 32°C (33). The experimental data from rabbit SA node cells with various values of C_m at 35°C (27) are similar to the experimental data from small balls of tissue from the periphery and center of the rabbit SA node at 32°C (33), although the action potential is shorter and the rate of spontaneous activity is faster in the single cells. We assume that these differences are the result of the higher temperature at which the experiments on single cells were conducted; for this reason, when model and experimental data were compared, more importance was placed on the data from single cells. In addition to this, the response of the simulated peripheral and central action potentials to block of various currents was calculated and compared with the experimentally measured response of peripheral and central action potentials to various blockers. If there were differences, we adjusted the densities of appropriate currents until the simulated and experimental results were more similar. Although the current densities in the models were adjusted in this manner, the final current densities had to be consistent with current densities measured experimentally (the scope for change was, therefore, limited). The models finally developed do not produce action potentials that are exact matches of any one experimental recording; instead, the action potentials have characteristics within the range observed experimentally and behaviors to ion channel block within the range observed experimentally.

One-Dimensional Model of the SA Node and Surrounding Atrial Muscle

On the basis of the models developed for peripheral and central SA node cells, a one-dimensional, partial differential equation, multicellular model for the SA node and atrium was developed. The equations for the one-dimensional model are listed in Table 13. In the model the multicellular SA node and atrium are modeled as a string of tissue with a length (L) of 12.6 mm; of this the string of SA node tissue has a length (L^s) of 3 mm [similar to the distance from the center of the SA node to the atrial muscle in the rabbit (3)], and the string of atrial tissue has a length of 9.6 mm. It could be argued that a two-dimensional model of the SA node and atrium as used by others would be more appropriate. However, the one-dimensional model is computationally more efficient, and, furthermore, in a radially symmetrical, two-dimensional model of a circular SA node within a concentric atrium, the behavior of a string of tissue extending from the center of the SA node to atrial muscle will be no different from the one-dimensional model described here, because there will be no net current flow laterally (i.e., at a tangent to the propagating wavefront of the action potential) in the one- or the two-dimensional model. Within the string of SA node tissue, we assume that C_m changes from 20 pF (C_m in the central SA node cell model) to 65 pF (C_m in the peripheral SA node cell model) exponentially (Eq. 80, Table 13) and ionic current conductances are functions of C_m (Eq. 81, Table 13). In the model, single atrial cells are represented by the Earm-Hilgemann-Noble equations (48). Electrotonic interactions within the tissue are modeled by the diffusive interactions of membrane potentials (Eqs. 82 and 83, Table 13). We used nonflux

Table 13. *One-dimensional model of the intact SA node*

For $x = 0-3$ mm

$$\left. \frac{dV^s}{dn} \right|_{x=0} = 0 \quad (79)$$

$$C_m^s(x) = 20 + \frac{1.07(x - 0.1)}{L^s[1 + 0.7745e^{-(x - 2.05)/(0.295)}]} (65 - 20) \quad (80)$$

$$g^s(x) = \frac{[65 - C_m^s(x)]g_c + (C_m^s - 20)g_p}{65 - 20} \quad (81)$$

$$\frac{dV^s(x)}{dt} = -\frac{1}{C_m^s(x)} \left[i_{tot}^s(x) + D^s \frac{d^2 V^s(x)}{dx^2} \right] \quad (82)$$

For $x = 3-12.6$ mm

$$\frac{dV^a(x)}{dt} = -\frac{1}{C_m^a(x)} \left[i_{tot}^a(x) + D^a \frac{d^2 V^a(x)}{dx^2} \right] \quad (83)$$

$$\left. \frac{dV^a}{dn} \right|_{x=L} = 0 \quad (84)$$

boundary conditions for both ends of the model (Eqs. 79 and 84, Table 13). D^s and D^a scale the conduction velocity of the action potential in the SA node and the atrial muscle. The conduction velocity for near-planar waves is $\sim 0.001-0.1$ m/s in the SA node and $\sim 0.3-0.8$ m/s in the atrium (20). We set D^s at 0.6 cm²/s, which gives a conduction velocity of ~ 0.06 m/s in the SA node, and D^a at 1.25 cm²/s, which gives a conduction velocity of 0.62 m/s in the atrial muscle. Coupling at the junction of the SA node and atrial muscle is by the diffusion coefficient (D^s).

Computational Methods

The models were coded in C and Fortran languages. The programs were run on Indigo 2, Silicon Graphics machines with an IRIS 6.0 operating system. A fourth-order Runge-Kutta-Merson numerical integration method (55) was used to solve the ordinary differential equations. The time step was 0.1 ms, which gives a stable solution of the equations and maintains the accuracy of the computation of membrane current and potential. One-dimensional partial differential equations were solved by an explicit Euler method with a three-node approximation of the Laplacian operator (55), with a time step of 0.1 ms and a space step of 0.1 mm for SA node tissue and 0.32 mm for atrial muscle. The chosen time and space steps are sufficiently small for a stable and accurate solution.

RESULTS

Peripheral and Central SA Node Action Potentials

Figure 6 shows the action potentials generated using the models of a peripheral cell ($C_m = 65$ pF) and a central cell ($C_m = 20$ pF) at 37°C from the SA node of the rabbit at fast (Fig. 6A) and slow (Fig. 6B) time bases. For comparison, Fig. 6 also shows action potentials recorded experimentally from rabbit SA node preparations: Figure 6C shows action potentials at a fast time base recorded from small balls of tissue from the periphery and center of the SA node at 32°C, and Fig. 6D shows action potentials at a slow time base

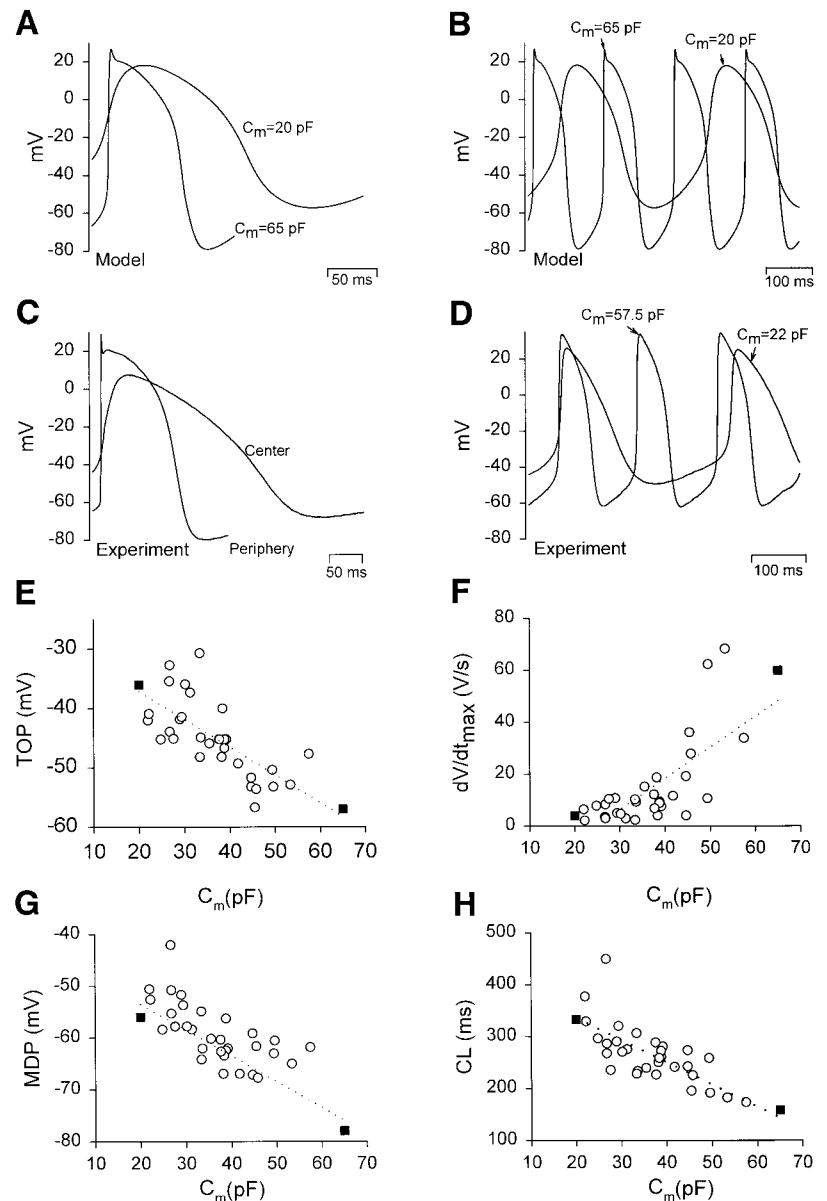


Fig. 6. Simulated peripheral and central SA node action potentials. *A*: simulated action potentials at a fast time base. *B*: simulated action potentials at a slow time base. *C*: action potentials recorded from small balls of peripheral and central rabbit SA node tissue (balls *B* and *D*) at a fast time base (unpublished observations). *D*: action potentials recorded from rabbit SA node cells with C_m of 57.5 and 22.0 pF at a slow time base (unpublished observations). *E*–*H*, takeoff potential (TOP; *E*), maximum upstroke velocity (dV/dt_{max} ; *F*), maximum diastolic potential (MDP; *G*) and cycle length (CL; *H*) plotted against C_m . \circ , Data from Honjo et al. (27) from rabbit SA node cells; dotted lines, regression lines; \blacksquare , values computed from the peripheral ($C_m = 65$ pF) and central ($C_m = 20$ pF) SA node cell models.

recorded from single cells with C_m of 57.5 and 22.0 pF at 35°C. The simulated action potentials are similar to those recorded experimentally. The action potential of the peripheral model has a more negative takeoff potential, a more rapid upstroke, a more positive peak value, a greater amplitude, a shorter duration, and a more negative maximum diastolic potential than the action potential of the central model. Furthermore, the spontaneous activity of the peripheral model is faster than that of the central model. All these are characteristic differences seen experimentally between small balls of tissue from the periphery and center of the rabbit SA node (31, 33) or large and small rabbit SA node cells (27) (Fig. 6, *C* and *D*). The action potential from the peripheral model has an early rapid phase of repolarization (phase 1) after the action potential upstroke. Such an early rapid phase of repolarization after the action potential upstroke can be observed

frequently in the periphery of the intact SA node (but not in the center) and in small balls of tissue from the periphery (but not from the center) (6, 34, 45) (Fig. 6*C*).

Figure 6, *E*–*H*, compares the characteristics of the simulated action potentials with the average characteristics of action potentials recorded experimentally from rabbit SA node cells by Honjo et al. (27) at 35°C. The open circles in Fig. 6, *E*–*H*, show experimental measurements of the takeoff potential, maximum upstroke velocity, maximum diastolic potential, and cycle length (time between successive spontaneous action potentials) of rabbit SA node cells plotted against C_m . In all cases, there are significant correlations of the variables with C_m (27). In Fig. 6, *E*–*H*, the filled squares show corresponding values from the peripheral and central models. In all cases, the model values are close to those recorded experimentally; the changes with C_m are also comparable to those seen experimen-

tally. There is also a significant correlation between action potential amplitude and C_m in rabbit SA node cells [action potential amplitude is greater in larger cells (27)], and once again corresponding values from the peripheral and central models are comparable (not shown). Although Honjo et al. observed no significant correlation between action potential duration and C_m in rabbit SA node cells, there is a difference in action potential duration between the peripheral and central models (Fig. 6A). However, the action potential durations in the peripheral and central models are still comparable to the data from rabbit SA node cells (not shown), and, furthermore, in small balls of tissue from the periphery and center of the rabbit SA node, a significant regional difference in action potential duration is observed (Fig. 6C) (5) similar to that between the peripheral and central models (Fig. 6A).

The takeoff potential, maximum upstroke velocity, peak value of the action potential, action potential amplitude, maximum diastolic potential, and cycle length in the peripheral and central models are comparable to experimental data obtained from small balls of tissue from the periphery and center of the rabbit SA node (33). However, in the case of the data from the small balls of tissue (at 32°C), the action potential duration and cycle length are longer than in the peripheral and central models (37°C) and also longer than in single cells (obtained at 35°C) (27). This may be the result of the lower temperature of 32°C used in the work on the small balls of tissue (33).

Figure 7 shows changes in various ionic currents

(i_{Na} , $i_{Ca,L}$, i_{to} , $i_{K,r}$, $i_{Ca,T}$, $i_{K,s}$, and i_f) during the action potentials generated by the peripheral and central models. Because of the regional differences in ionic current densities and C_m described above, the amplitudes of the ionic currents are different in the peripheral and central models. The changes in $i_{Ca,L}$, $i_{K,r}$, and i_f during the action potential are comparable in amplitude and time course to the changes in the three currents during the action potential in rabbit SA node cells as measured with the action potential-clamp technique (62).

Effect of Block of Ionic Currents

In the absence of voltage-clamp data from single cells isolated from the different regions of the SA node, voltage-clamp data from single SA node cells of different size (as measured by C_m) have been used as described above. However, this relies on the assumption that C_m is a good indicator of the origin of the cell in the intact SA node. A second source of data concerning regional differences within the SA node has been small balls of tissue from the different regions. In this case, the origin of the tissue is not in question. Although it is not possible to obtain voltage-clamp data from small balls of tissue from different regions, information about regional differences in ionic currents can be inferred by investigating the effects of ion channel blockers. In this section, the effects of block of various ionic currents in the models (37°C) are compared with the effects ob-

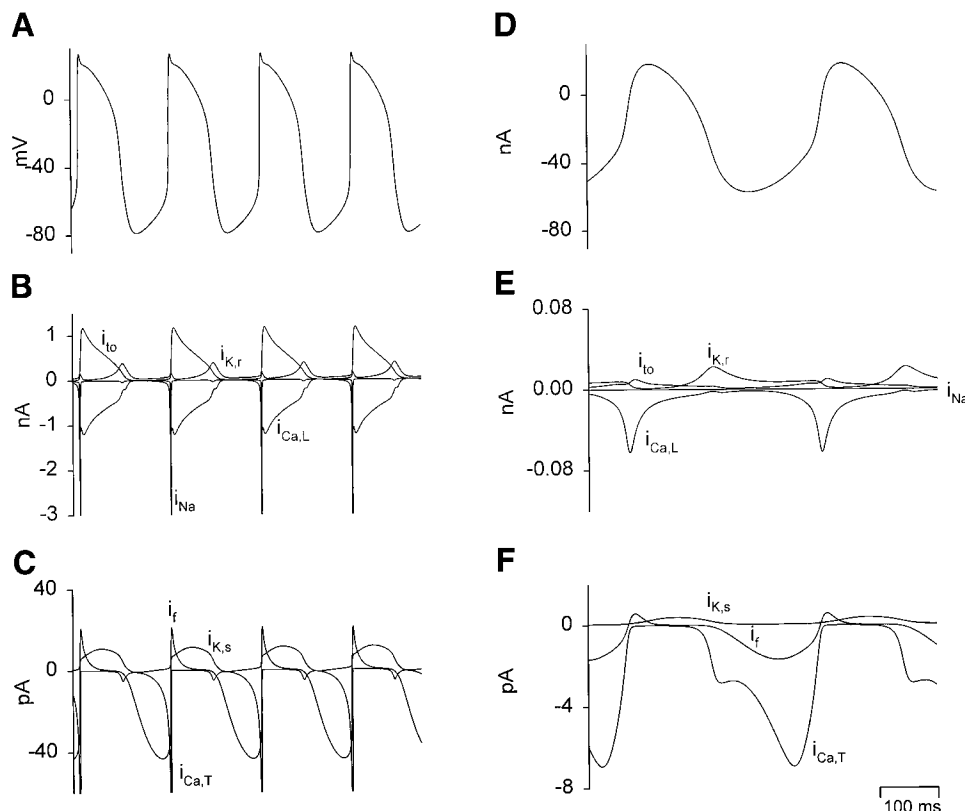


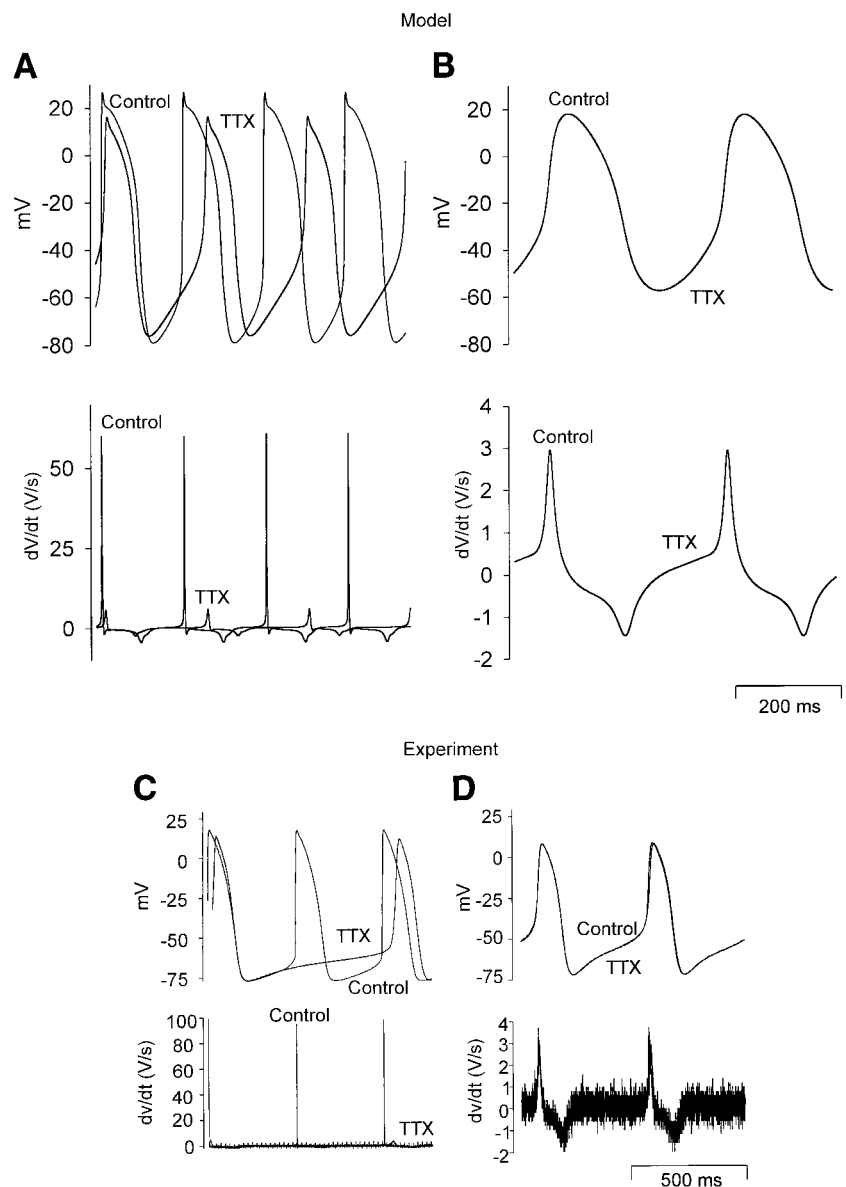
Fig. 7. Simulated peripheral (A–C) and central (D–F) SA node action potentials (A and D) and underlying ionic currents (B and E: i_{Na} , $i_{Ca,L}$, i_{to} , and $i_{K,r}$; C and F: $i_{Ca,T}$, $i_{K,s}$, and i_f).

served experimentally in small balls of tissue from the rabbit SA node (32°C).

Effect of block of i_{Na} . Figure 8, *A* and *B*, shows the effect of block of i_{Na} on the action potential of the peripheral and central models. Figure 8, *C* and *D*, shows the effect of block of i_{Na} by 20 μ M TTX on action potentials recorded from peripheral and central balls of rabbit SA node tissue (33). Qualitatively, the models behave in the same way as the tissue. In both cases (simulation and experiment), blocking i_{Na} had no effect on the central action potential. In the simulation, at least, this is because there is no i_{Na} in the central model. In contrast, blocking i_{Na} had various effects on the peripheral action potential: 1) the takeoff potential was shifted to a more positive value; 2) the maximum upstroke velocity was reduced (in the example of experimental data the maximum upstroke velocity was reduced from 100 to 5 V/s, and in the simulation it was reduced from 60 to 8 V/s; after block of i_{Na} , in simula-

tion and experiment, the upstroke velocity in the periphery was approximately the same as that in the center); and 3) as a result of the change in the takeoff potential, spontaneous activity was slowed. In the model at least, the effects of block of i_{Na} can be explained by the important role of i_{Na} in the upstroke of the peripheral action potential. The effect of block of i_{Na} on spontaneous activity was less in the peripheral model than that seen experimentally in peripheral tissue (Fig. 8); this difference may be the result of the faster spontaneous activity of the peripheral model (which, in turn, may be the result of the model being developed for 37°C and the experimental data being obtained at 32°C). In the peripheral model, block of i_{Na} also reduced the peak value of the action potential, the action potential duration, and the maximum diastolic potential (Fig. 8*A*); these changes are also seen experimentally in small balls of tissue from the periphery of the rabbit SA node (Fig. 8*C*) (33). In conclusion, in

Fig. 8. Effect of block of i_{Na} on peripheral (*A* and *C*) and central (*B* and *D*) SA node action potentials. *A* and *B*: data from peripheral and central SA node cell models. *C* and *D*: data from Kodama et al. (33) from small balls of peripheral and central rabbit SA node tissue (balls *A* and *D*). *Top panels*: membrane potential; *bottom panels*: rate of change of membrane potential (dV/dt). Data are shown under control conditions and after block of i_{Na} (TTX). In experiments, 20 μ M TTX was used to block i_{Na} .



simulation and experiment, pacemaking in the periphery, unlike that in the center, is sensitive to block of i_{Na} .

Effect of block of $i_{Ca,L}$. Figure 9, *A* and *B*, shows the effect of the block of $i_{Ca,L}$ on the action potential of the peripheral and central models. Figure 9, *C* and *D*, shows the effect of block of $i_{Ca,L}$ by 2 μ M nifedipine on action potentials recorded from peripheral and central balls of rabbit SA node tissue (33). Qualitatively, the models behave in the same way as the tissue. In both cases (simulation and experiment), block of $i_{Ca,L}$ abolished the action potential in the center of the SA node: the membrane potential settled at -45 mV in the experiment (Fig. 9*D*) and at -42 mV in the simulation (Fig. 9*B*). In the periphery, block of $i_{Ca,L}$ had different effects on electrical activity. In both cases (simulation and experiment), block of $i_{Ca,L}$ 1) shortened the action potential, 2) increased the pacemaking rate [presum-

ably as a consequence of the shortening of the action potential; in the simulation, block of $i_{Ca,L}$ caused a 22% increase in the pacemaking rate; in experiments, 2 μ M nifedipine caused a $21 \pm 1\%$ (SE) increase in the pacemaking rate in ball *A* (33)], 3) decreased the maximum upstroke velocity, and 4) decreased the peak value of the action potential. In the simulation, block of $i_{Ca,L}$ caused a decrease in the maximum upstroke velocity from 60 to 40 V/s and a decrease in the peak of the action potential from $+27$ to $+8$ mV. In the experiment shown in Fig. 9*C*, on application of 2 μ M nifedipine, the maximum upstroke velocity was decreased from 82 to 75 V/s and the peak of the action potential was decreased from $+22$ to $+6$ mV. In conclusion, in simulation and experiment, only pacemaking in the center is abolished on block of $i_{Ca,L}$.

Effect of block of $i_{Ca,T}$. Hagiwara et al. (22) reported that block of $i_{Ca,T}$ by 40 μ M Ni^{2+} produced a 5–15%

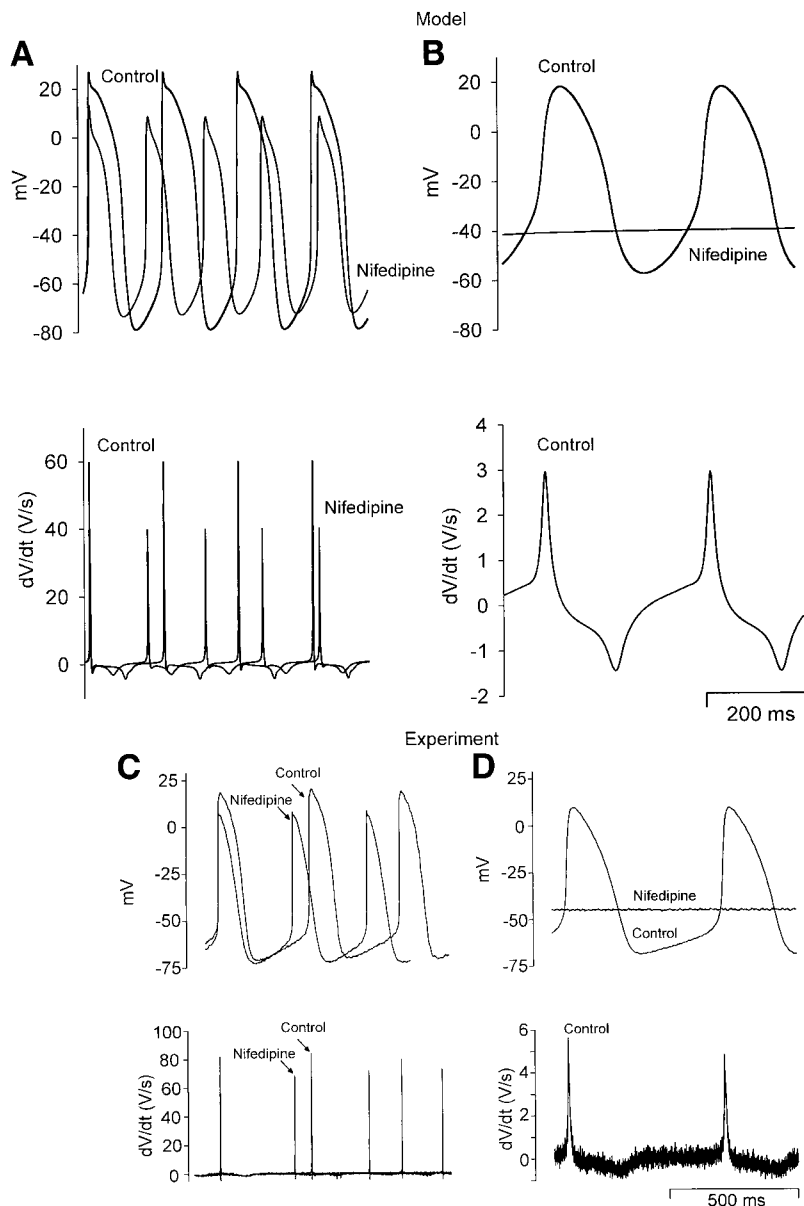


Fig. 9. Effect of block of $i_{Ca,L}$ on peripheral (*A* and *C*) and central (*B* and *D*) SA node action potentials. *A* and *B*: data from peripheral and central SA node cell models. *C* and *D*: data from Kodama et al. (33) from small balls of peripheral and central rabbit SA node tissue (balls *A* and *D*). Top panels: membrane potential; bottom panels: rate of change of membrane potential. Data are shown under control conditions and after block of $i_{Ca,L}$ (nifedipine). In experiments, 2 μ M nifedipine was used to block $i_{Ca,L}$.

increase in the cycle length in rabbit SA node cells, and Lei et al. (38) reported a similar effect in rabbit SA node cells. No information is available from single cells or small balls of tissue on whether the effect of block of $i_{Ca,T}$ differs in peripheral and central SA node tissue. Because there is also no information available on whether the density of $i_{Ca,T}$ differs in peripheral and central SA node cells, the density of $i_{Ca,T}$ is assumed to be the same in the two cell types (see MODEL DEVELOPMENT). In the peripheral and central models, block of $i_{Ca,T}$ caused a small increase in cycle length (of 4 and 19%, respectively) similar to that reported experimentally.

Effect of block of 4-AP-sensitive current. Figure 10, A–C, shows the effect of block of 4-AP-sensitive current (i_{to} and i_{sus}) on peripheral and central action potentials. 4-AP has also been shown to block $i_{K,r}$ partially (J. Hancox, unpublished observations). In the simulation of the effect of 4-AP, $i_{K,r}$ was blocked by 10%. Figure 10, A and B, shows the effect of block of 4-AP-sensitive current on the action potential of the peripheral and central models. Figure 10C shows

the effect of 5 mM 4-AP on action potentials recorded from peripheral and central balls of rabbit SA node tissue (6). Qualitatively, the models behave in the same way as the tissue. In both cases (simulation and experiment), block of 4-AP-sensitive current caused a prolongation of the action potential in the periphery and center. In experiments, 4-AP increased action potential duration by $66 \pm 4\%$ in peripheral tissue and by $25 \pm 5\%$ in central tissue (Ref. 6; data from *balls A* and *E* are quoted). In simulations, block of 4-AP-sensitive current caused a 50% increase in action potential duration in the peripheral model and a 21% increase in the central model. Block of 4-AP-sensitive current also caused an increase in the peak value of the action potential, an increase in cycle length in the periphery, and a decrease in cycle length in the center. In experiments, 4-AP caused a $28 \pm 3\%$ increase in cycle length in peripheral tissue and a $5 \pm 2\%$ decrease in cycle length in central tissue (Ref. 6; data for *balls A* and *D* are quoted). In simulations, 4-AP caused a 24% increase in cycle length in the peripheral model

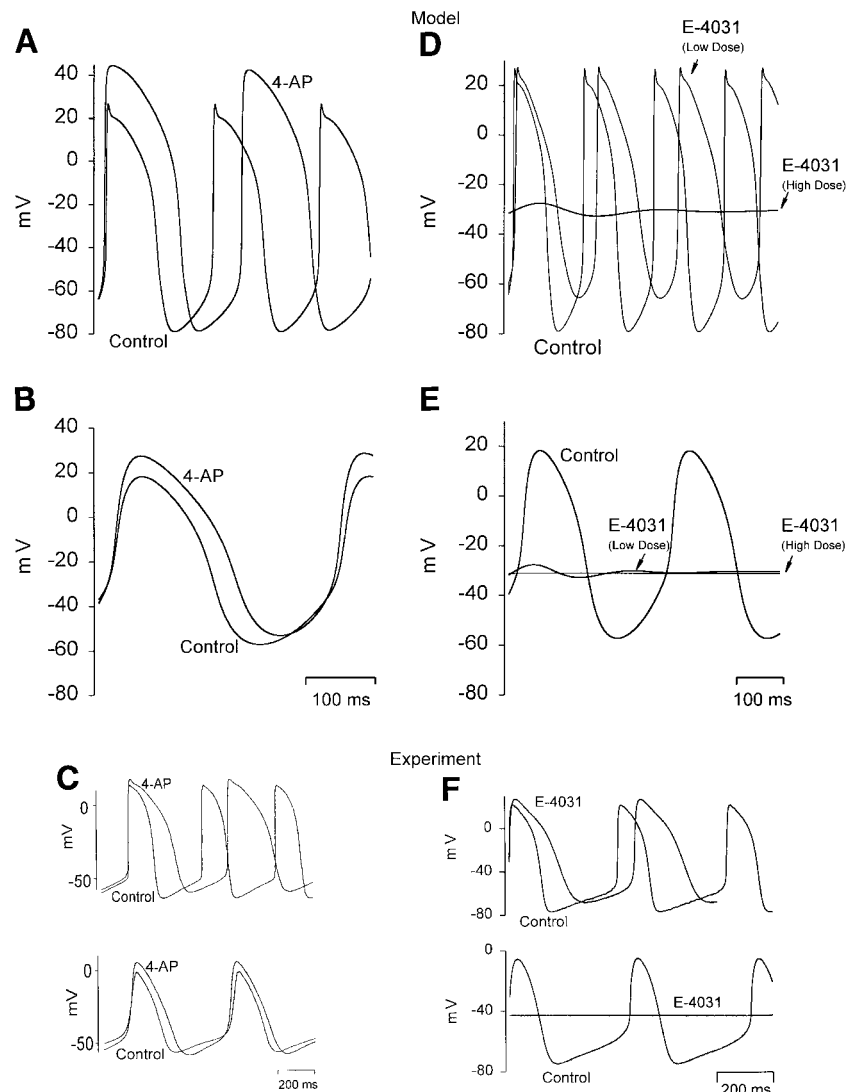


Fig. 10. Effect of block of 4-AP-sensitive current and $i_{K,r}$ on peripheral and central SA node action potentials. A and B: effect of block of 4-AP sensitive current on the peripheral (A) and central (B) SA node cell models. C: effect of 5 mM 4-AP on small balls of peripheral (top) and central (bottom) rabbit SA node tissue [*balls A* and *D*; from Boyett et al. (6)]. D and E: effect of block of $i_{K,r}$ by 50 and 100% (equivalent to low and high doses of E-4031) on the peripheral (D) and central (E) SA node cell models. F: effect of 0.1 μ M E-4031 [a low dose of E-4031 expected to block $\sim 50\%$ of $i_{K,r}$ (32)] on small balls of peripheral (top) and central (bottom) rabbit SA node tissue [*balls B* and *F*; from Kodama et al. (32)]. Data are shown under control conditions and after block of 4-AP-sensitive current (4-AP) or $i_{K,r}$ (E-4031).

and a 3% decrease in cycle length in the central model. As discussed above, in experiments on the rabbit SA node, in some cases, after the upstroke of the action potential in the periphery there can be an initial rapid phase of repolarization (i.e., phase 1) (however, not in the experimental recording shown in Fig. 10C), and in such cases this was abolished by 4-AP (6). In the peripheral model, the initial rapid phase of repolarization was also abolished by block of 4-AP-sensitive current (Fig. 10A). In summary, simulations and experiments show that 4-AP-sensitive current plays a major role in action potential repolarization, and its role varies regionally.

In simulations in which i_{to} and i_{sus} were blocked only (i.e., $i_{K,r}$ was not blocked by 10%), the changes were similar: in the peripheral model, the action potential duration was increased by 49% (rather than by 50%), the maximum diastolic potential was changed by -1 mV (rather than by $+0.5$ mV), and the cycle length was increased by 26% (rather than by 24%); in the central model, the action potential duration was increased by 19% (rather than by 21%), the maximum diastolic potential was changed by $+0.9$ mV (rather than by $+5.7$ mV), and the cycle length was decreased by 1.5% (rather than by 3%).

Effect of block of $i_{K,r}$. Figure 10, D and E, shows the effect of the block of 50 and 100% $i_{K,r}$ (simulating the effects of low and high doses of E-4031) on the action potential of the peripheral and central models. Figure 10F shows the effect of partial block (perhaps $\sim 50\%$) (32) of $i_{K,r}$ by $0.1 \mu\text{M}$ E-4031 on action potentials

recorded from peripheral and central balls of rabbit SA node tissue (33). Qualitatively, the models behave in the same way as the tissue. In both cases [simulation (Fig. 10, D and E) and experiment (not shown; see Ref. 32)], complete block of $i_{K,r}$ (in experiments, by $1 \mu\text{M}$ E-4031) caused cessation of spontaneous activity in the periphery and center. After complete block of $i_{K,r}$, the membrane potential settled at -35 ± 2 mV in rabbit peripheral SA node tissue (Ref. 32, data for *ball A*), -32 ± 2 mV in rabbit central SA node tissue (Ref. 32, data for *ball D*), -33 mV in the peripheral model, and -30 mV in the central model. This shows that in the periphery and center, $i_{K,r}$ is important for pacemaking. The $i_{K,r}$ is responsible for generating the maximum diastolic potential, and thus when $i_{K,r}$ is blocked, the membrane during diastole is depolarized and spontaneous activity ceases.

Partial block of $i_{K,r}$ has different effects on the action potential in the periphery and center. In simulation ($i_{K,r}$ blocked by 50%) and experiment ($i_{K,r}$ partially blocked by $0.1 \mu\text{M}$ E-4031), partial block of $i_{K,r}$ abolished the action potential in the center but not in the periphery (Fig. 10, D–F). In both cases (simulation and experiment), in the periphery, partial block of $i_{K,r}$ 1) increased action potential duration, 2) decreased maximum diastolic potential, and 3) increased cycle length. This shows that the periphery of the SA node is more resistant to block of $i_{K,r}$ than the center. Kodama et al. (32) proposed that this is the result of a greater density of $i_{K,r}$ in peripheral cells than in central cells. In the models at least, the greater resistance of the peripheral

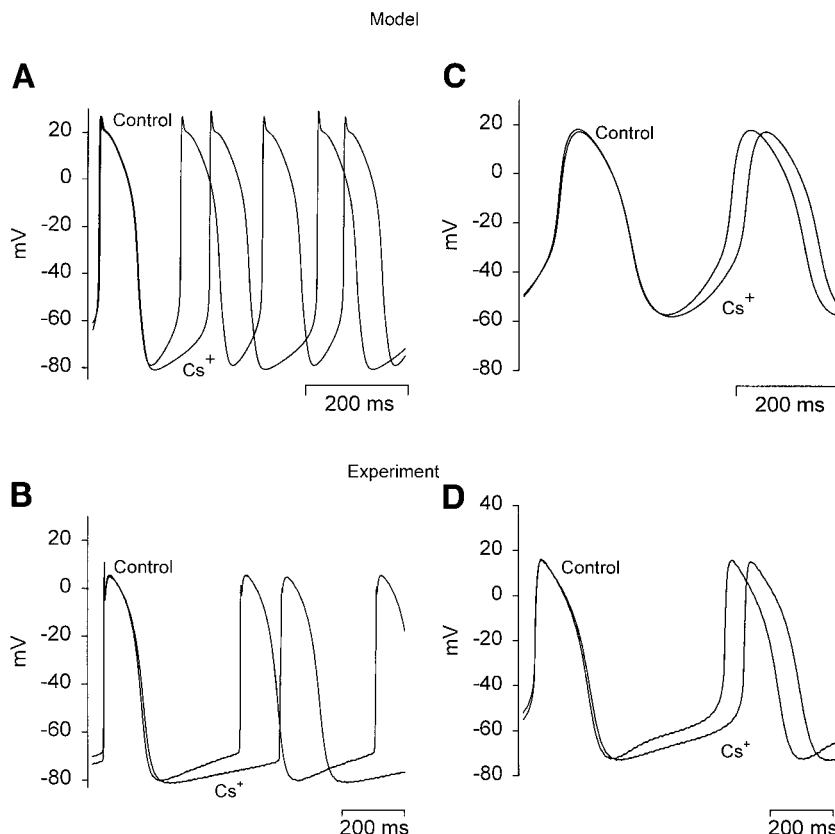


Fig. 11. Effect of block of i_f on peripheral (A and B) and central (C and D) SA node action potentials. A and C: data from peripheral and central SA node cell models. B and D: data from Nikmaram et al. (45) from small balls of peripheral and central rabbit SA node tissue (*balls A and D*). Data are shown under control conditions and after block of i_f (Cs^+). In experiments, 2 mM Cs^+ was used to block i_f .

model to partial block of $i_{K,r}$ is indeed the result of a greater density of $i_{K,r}$ in the peripheral model: in the peripheral model, if the density of $i_{K,r}$ was reduced to that in the central model, 50% block of $i_{K,r}$ abolished spontaneous activity (not shown).

Effect of block of $i_{K,s}$. Complete block of $i_{K,s}$ had little effect on the pacemaker activity of the peripheral and central models: there was a change in cycle length of 0.3 and 1% in the peripheral and central models. M. Lei and P. Kohl (unpublished observations) observed that block of $i_{K,s}$ by 50 μ M 293B had no significant effect on the electrical activity of rabbit SA node cells: cycle length was 256 ± 24 and 270 ± 26 (SE) ms ($n = 5$) under control conditions and in the presence of 293B, respectively.

Effect of block of i_f . Figure 11, A and C, shows the effect of block of i_f on the action potential of the peripheral and central models. Figure 11, B and D, shows the effect of block of i_f by 2 mM Cs^+ on action potentials recorded from peripheral and central balls of rabbit SA node tissue (45). Qualitatively, the models behave in the same way as the tissue. In both cases (simulation and experiment), block of i_f slowed spontaneous activity, and the slowing was greater in the periphery. In experiments, block of i_f caused a $24 \pm 2\%$ increase in cycle length in peripheral tissue and a $7 \pm 2\%$ increase in central tissue (Ref. 44, data for *balls A and D*), whereas in simulations, block of i_f caused a 34% increase in the cycle length in the peripheral model and an 8% increase in the central model. In the simulations, the greater effect of block of i_f on the peripheral model can be explained by the greater density of i_f in the peripheral model: in the peripheral model, if the density of i_f was reduced to that in the central model, block of i_f caused only a 14% increase in the cycle length.

Resting potentials. In simulation and experiment, blocking i_{Na} and $i_{Ca,L}$ (by 3 μ M TTX and 6 μ M nifedipine, respectively, in experiments) or blocking $i_{K,r}$ (by 1 μ M E-4031 in experiments) abolished spontaneous activity in the periphery and center (32). After block of spontaneous activity, SA node cells settle at their resting potential. Figure 12 shows the maximum diastolic potential as well as the resting potentials in the peripheral and central models (Fig. 12A) and peripheral and central balls of rabbit SA node tissue (Fig. 12B) (32); the two sets of data are comparable. In simulation and experiment, whereas there was a substantial difference between the periphery and center in the maximum diastolic potential, there was a smaller difference between the two in the resting potential when spontaneous activity was terminated by block of i_{Na} and $i_{Ca,L}$ and little difference between the two in the resting potential when spontaneous activity was terminated by block of $i_{K,r}$. It was previously suggested that this showed that the difference in maximum diastolic potential between the periphery and center was the result of a difference in the density of $i_{K,r}$ between the two (32). Consistent with this, in the models, if the density of $i_{K,r}$ in the peripheral model was set to be the same as that in the central model, the difference in the

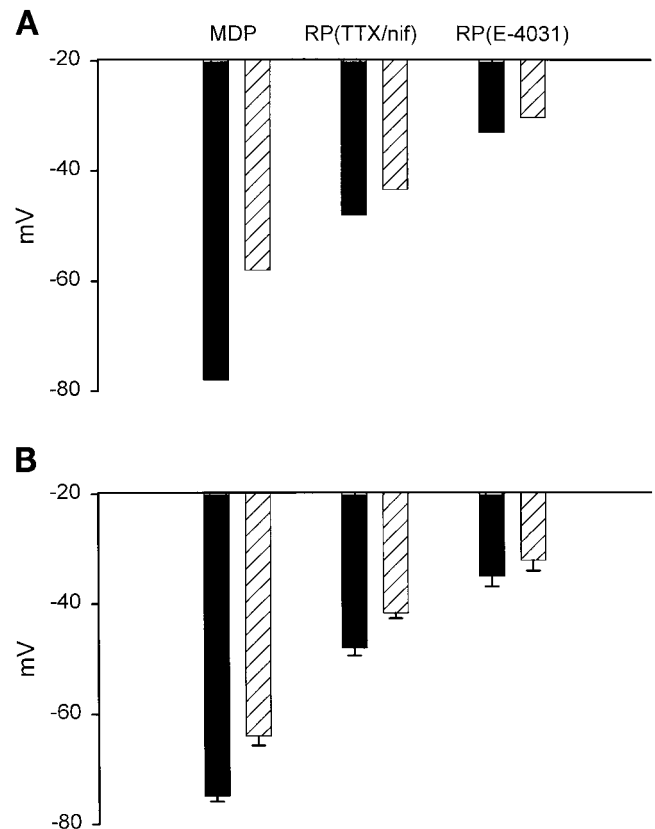


Fig. 12. Resting potentials in the periphery and center of the SA node. A: data from peripheral (solid bars) and central (hatched bars) SA node cell models. B: data from Kodama et al. (32) from small balls of peripheral (solid bars; *balls A and B*) and central (hatched bars; *balls D–F*) rabbit SA node tissue. Values are means \pm SE. MDP, maximum diastolic potential; RP(TTX/Nif), resting potential after block of spontaneous activity by block of i_{Na} and $i_{Ca,L}$; RP(E-4031), resting potential after block of spontaneous activity by block of $i_{K,r}$. In experiments, i_{Na} , $i_{Ca,L}$, and $i_{K,r}$ were blocked by 3 μ M TTX, 6 μ M nifedipine (Nif), and 1 μ M E-4031, respectively.

maximum diastolic potential was abolished (not shown; the maximum diastolic potential was -42 mV).

One-Dimensional Model of the Intact SA Node

Many of the properties of the intact SA node, for example, conduction, conduction disturbances, suppression of the SA node by the surrounding atrial muscle, and pacemaker shift, are the result of the multicellular nature of the SA node and the electrotonic interaction between the SA node and the atrial muscle surrounding the SA node. The intact SA node and the surrounding atrial muscle represent a complex structure, and an anatomically accurate model of the intact SA node is outside the scope of this study. However, the behavior of the intact SA node tissue can be qualitatively simulated by a simple model that ignores the complex structure of the SA node and idealizes the tissue as a one-dimensional string of tissue extending from the center of the SA node to the periphery and then onto atrial muscle (Fig. 13A). Within the string of SA node cells, C_m is assumed to change from 20 to 65 pF in an exponential fashion, and densities of

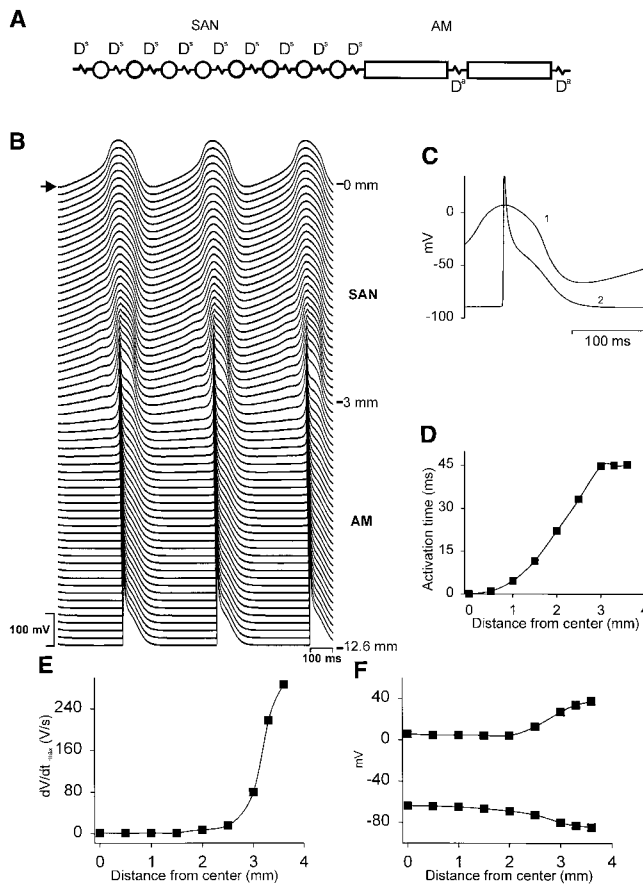


Fig. 13. One-dimensional model of the SA node. A: schematic diagram of part of the one-dimensional model. SAN, SA node; AM, atrial muscle; D^s and D^a , diffusion coefficients. B: action potentials recorded at regular intervals along the one-dimensional model from the center of the SA node (at 0 mm) to the junction of the SA node with the atrial muscle (3 mm) and into the atrial muscle (up to 12.6 mm from the center of the SA node). Arrow, point of initiation of the action potential (the leading pacemaker site). C: action potentials recorded from a central SA node cell (1) and an atrial cell (2) in the one-dimensional model. D–F: activation time (D), maximum upstroke velocity (dV/dt_{\max} , E), and peak value of the action potential and maximum diastolic potential (F) plotted against the distance from the center of the SA node.

ionic currents are functions of C_m . Electrotonic coupling between cells is determined by diffusion coefficients (D^s and D^a). The values of the diffusion coefficients were chosen to obtain appropriate conduction velocities within the SA node and atrial muscle (see MODEL DEVELOPMENT). D^s will also influence the effective space constant (λ) of the string of SA node tissue, and, therefore, λ was measured to determine whether the value of λ in the model is similar to that measured experimentally. A 2-ms current pulse was injected into an SA node cell 1 mm from the junction of the SA node with the atrial muscle. The current was injected during diastole to depolarize the cell at the point of injection by 17.5 mV. A similar technique has been used experimentally (4). The amplitude of the depolarization declined away from the point of injection in an exponential manner with a λ of 380 μm ; this compares with λ of 310–520 μm measured experimentally in the rabbit SA node by Bleeker et al. (4).

Figure 13B shows action potentials computed using the one-dimensional model of the intact SA node. Action potentials from various points along the string of tissue are shown. The junction of the SA node and atrium is at 3 mm. Figure 13B shows that spontaneous action potentials were first initiated in the center of the SA node (highlighted by the arrow) and then propagated to the periphery of the SA node and onto the atrial muscle. This is similar to the activation sequence seen experimentally (3). The cycle length in the one-dimensional model of the intact SA node is 350 ms; this is greater than the cycle length in the peripheral (160 ms) or central (330 ms) model. However, the cycle length in the one-dimensional model of the intact SA node is comparable to that observed experimentally in the intact SA node of the rabbit at 37°C: 348 ± 50 ms (30). Furthermore, at 33°C the cycle length in the intact SA node of the rabbit (586 ms) is greater than the cycle length in isolated peripheral (298 ± 8 ms) or central (331 ± 13 ms) tissue (Ref. 31, data for *balls A and D*). The SA node conduction time (time for the action potential to conduct out of the SA node) is 45 ms, similar to that seen experimentally (1). Figure 13C shows superimposed action potentials at a fast time base from the one-dimensional model: from the center of the SA node and the atrial muscle. Figure 13, D–F, shows various action potential parameters (activation time, i.e., the time taken for the action potential to propagate from the leading pacemaker site in the center, maximum upstroke velocity, peak value of the action potential, and maximum diastolic potential) plotted against the distance from the center of the SA node. The model data are comparable to experimental data (31). In summary, the one-dimensional model of the intact SA node shows a range of behaviors comparable to that of the intact SA node of the rabbit.

DISCUSSION

From the modeling, it is concluded that in the periphery compared with the center of the SA node 1) the takeoff potential is more negative and the maximum upstroke velocity is higher as a result of a higher density of i_{Na} , 2) the action potential can have a notch as a result of a higher density of i_{to} , 3) the action potential is short as a result of higher densities of $i_{\text{K,r}}$ and 4-AP-sensitive current, 4) the maximum diastolic potential is more negative principally as a result of a higher density of $i_{\text{K,r}}$, and 5) the spontaneous activity is faster as a result of higher densities of i_{Na} and i_f as well as the shorter action potential.

After the pioneering work of Noble (47), much effort has been devoted to the development of mathematical models of cardiac cells based on voltage-clamp data. With the development of computing power and resources, these models, together with information about the structure of cardiac tissue, the electrical coupling between cells, cell orientation, and the heterogeneity in the electrophysiological properties of cardiac cells, are being used to develop biophysically accurate and detailed mathematical models of cardiac tissues (54); the

aim is to develop a model of the whole heart. It is hoped that the models developed in the present study of action potentials in the periphery and center of the SA node can be used to develop a two- or three-dimensional model of the intact SA node, which then can be used in the development of a whole heart model.

Comparison With Previous Models

The models developed have a structure similar to previous SA node models (13, 49, 59). However, because of recent experimental findings, we have been able to update the previous models in many ways. Formulations for various currents have been updated, and currents not included in previous models (or currents not correctly modeled because of the absence of data) have been introduced: i_{Na} [although i_{Na} was included in a previous model, the equations used were not based on data from rabbit SA node cells, and the time course of i_{Na} during the action potential is inappropriate (13)], 4-AP-sensitive current (i_{to} and i_{sus}), and two components of i_K ($i_{K,r}$ and $i_{K,s}$). A major advance on previous models is the introduction of separate models for peripheral and central SA node cells. Although Noble and Noble (49) developed separate models of peripheral and central cells, the postulated underlying differences in ionic currents had to be based on speculation, whereas in the present study the differences could be based on experimental data. In the present study, the models were tested by investigating the effect of block of various ionic currents (i_{Na} , $i_{Ca,L}$, $i_{Ca,T}$, 4-AP-sensitive current, $i_{K,r}$, $i_{K,s}$, and i_f). With previous models, only the effect of block of $i_{Ca,T}$ and i_f has been reported (9, 13, 38, 59). With one model (13), the effect of block of $i_{Ca,T}$ is not the same as in experiments. In the present study, the models were also tested by measuring resting potentials after block of spontaneous activity; resting potentials in previous models have not been reported. Furthermore, in two of the models at least (13, 49), block of spontaneous activity by block of i_K results in a resting potential of ~ 0 mV (unpublished observations), rather than a resting potential of -32 to -35 mV measured experimentally on blocking $i_{K,r}$ (32).

Achievements of the New Models

The action potentials from the peripheral and central SA node cell models are comparable to action potentials recorded from peripheral and central tissue from the rabbit SA node (5, 6, 31, 33) as well as those of large and small rabbit SA node cells (Fig. 6). As discussed in MODEL DEVELOPMENT, the models are based on current densities of rabbit SA node cells of different C_m rather than cells isolated from the periphery and center of the SA node. It had to be assumed that C_m is an indicator of the region of origin of cells. The result that the action potentials from the peripheral and central SA node cell models are comparable to action potentials recorded from peripheral and central SA

node tissue from the rabbit (as well as to action potentials from large and small rabbit SA node cells) validates this assumption. Experimental work has shown that block of i_{Na} , 4-AP-sensitive current, and i_f has greater effects in peripheral rabbit SA node tissue, whereas block of $i_{Ca,L}$ and $i_{K,r}$ has greater effects in central rabbit SA node tissue (6, 32, 33, 45). From this indirect evidence, it was argued that this shows that the densities of i_{Na} , 4-AP-sensitive current, $i_{K,r}$, and i_f are greater in the periphery than in the center (6, 32, 33, 45). The modeling was able to support this interpretation, because in the peripheral and central SA node cell models, in which the densities of i_{Na} , 4-AP-sensitive current, $i_{K,r}$, and i_f are greater in the periphery than in the center, the effects of block of these currents as well as $i_{Ca,L}$ (Figs. 8–11) are qualitatively similar to those seen experimentally. Block of $i_{Ca,L}$ is a special case: block of $i_{Ca,L}$ has a greater effect on the center than on the periphery as a result, in the simulations at least, of the absence of i_{Na} in the center (in the peripheral model, after block of $i_{Ca,L}$, i_{Na} is able to support the action potential). When developing the models, to simulate peripheral and central SA node action potentials and the differential effect of partial block of $i_{K,r}$ by $0.1 \mu\text{M}$ E-4031 on peripheral and central action potentials (Fig. 10), we had to assume that the density of $i_{K,r}$ in a peripheral cell is substantially greater than that in a central cell (Fig. 4J); this was a prediction of the modeling. Subsequently, we measured the density of $i_{K,r}$ and confirmed the predicted densities of $i_{K,r}$ as shown in Fig. 4J.

The fact that the densities of i_{Na} , 4-AP-sensitive current (i_{to} and i_{sus}), $i_{K,r}$, $i_{K,s}$, i_f , and possibly $i_{Ca,L}$ (see MODEL DEVELOPMENT) decrease with a reduction of C_m and, therefore, possibly from the periphery to the center raises the possibility that the density of all currents decreases from the periphery to the center in the same way. Beyond the center (toward the interatrial septum) is a region of conduction block (see the introduction). Block of conduction is known to be the result of the loss of excitability rather than poor coupling between cells (4). It is possible that the loss of excitability is the result of a further decrease in the density of currents beyond the center (67).

Limitations of the Models

Any model will have limitations. The limitations of the present models include the 1) lack of information about the relationship between the density of some ionic currents and C_m in the rabbit SA node, 2) need to use data from rabbit SA node cells of different C_m rather than cells directly isolated from the different regions of the rabbit SA node, 3) need to use, in some instances, data from cardiac preparations other than rabbit SA node cells, 4) need to use, in some instances, data collected at temperatures $<37^\circ\text{C}$, 5) uncertainty about the accuracy of the experimental source data, 6) lack of some currents known to play important roles in the rabbit SA node, for example, the sustained current (i_{st}), the ACh-activated K^+ current ($i_{K,ACh}$), and the

ATP-sensitive K^+ current ($i_{K,ATP}$), 7) lack of Ca^{2+} -dependent inactivation of $i_{Ca,L}$, despite the fact that it is known to be present in the rabbit SA node (10), and 8) lack of intracellular Na^+ and Ca^{2+} regulation. Another limitation of the present study is that peripheral-central differences only in the rabbit SA node have been considered; there are also differences between the superior and inferior regions of the rabbit SA node, and the electrical activity in the zone of conduction block (between the leading pacemaker site in the center and the atrial muscle of the interatrial septum) is unique (4, 5). Quantitatively, there are differences in the effect of blocking of ionic currents on the action potentials in simulation and experiment. These differences may be due to the different temperatures used in the simulations and experiments, incomplete experimental data on the kinetics of ionic currents in rabbit SA node cells, poor selectivity of the agents used experimentally to block ionic currents, or one of the shortcomings just highlighted. Despite the limitations, the models presented here represent significant improvements on the earlier models and could be the basis for future developments, for example, of models of electrical activity in the superior and inferior regions and region of conduction block.

Model of the Intact SA Node

It is known that the multicellular nature of the rabbit SA node has a major influence on the behavior of the SA node (30, 31). Ultimately, it is an important goal to develop a two-dimensional and, perhaps, a three-dimensional model of the SA node. As a first step, we have developed a one-dimensional model of a string of SA node tissue (incorporating regional differences in the ionic current densities from the periphery to the center) coupled to a string of atrial tissue (Fig. 13). The one-dimensional model is a reasonable approximation of the intact SA node (see MODEL DEVELOPMENT). The one-dimensional model shows behavior similar to the intact SA node of the rabbit in terms of action potential profiles, action potential characteristics, rate of spontaneous activity, the action potential first being initiated in the center of the SA node, the space constant of the SA node, and the conduction velocity of the SA node (Fig. 13).

The intrinsic pacemaker activity of peripheral tissue from the rabbit SA node is faster than that of central tissue (33). Similarly, the pacemaker activity of large rabbit SA node cells is faster than that of small cells (27). However, in the intact SA node, the spontaneous action potential is first initiated in the center of the SA node (31). This is the result of the electrotonic suppression of the periphery of the SA node by the surrounding more hyperpolarized atrial muscle (the center of the SA node, being further from the atrial muscle, is less suppressed). The principal evidence for this is that if the atrial muscle is cut away from the rabbit SA node, the leading pacemaker site shifts to the periphery and the cycle length decreases on average from 350 to 290

ms (30). In the simulations, comparable behavior is observed. The spontaneous activity of the peripheral SA node cell model is faster than that of the central cell SA node model (Fig. 6), but in the one-dimensional model of the intact SA node it is the center that is the leading pacemaker site (Fig. 13). As in experiments, in the one-dimensional model, if the string of SA node tissue is uncoupled from the atrial tissue, the leading pacemaker site shifts to the peripheral cells and the cycle length decreases from 350 to 160 ms (not shown). Similar behavior has also been seen in earlier models of the intact SA node (60, 66).

The one-dimensional model of the rabbit SA node is already proving to be a useful tool: in preliminary studies we have shown pacemaker shift in the model, obtained data that suggest that i_{Na} in the periphery of the SA node helps the SA node drive the atrial muscle surrounding it, obtained data on the basis of which we have put forward a hypothesis to explain the deterioration of the SA node with age, and tested a hypothesis to explain the region of conduction block (63–65, 67). Although the one-dimensional model is a computationally efficient method of exploring the behavior of the intact SA node, it is only an approximation of the intact SA node, and in the future a more realistic model will have to be constructed, for example, to explore the asymmetric conduction of action potentials from the leading pacemaker site within the SA node.

This work was supported by a Programme Grant from the British Heart Foundation.

REFERENCES

1. **Alings AMW and Bouman LN.** Electrophysiology of the ageing rabbit and cat sinoatrial node—a comparative study. *Eur Heart J* 14: 1278–1288, 1993.
2. **Baruscotti M, DiFrancesco D, and Robinson RB.** A TTX-sensitive inward sodium current contributes to spontaneous activity in newborn rabbit sino-atrial node cells. *J Physiol (Lond)* 492: 21–30, 1996.
3. **Bleeker WK, Mackaay AJC, Masson-Pevet M, Bouman LN, and Becker AE.** Functional and morphological organization of the rabbit sinus node. *Circ Res* 46: 11–22, 1980.
4. **Bleeker WK, Mackaay AJC, Masson-Pevet M, Op't Hof T, Jongasma HJ, and Bouman LN.** Asymmetry of the sino-atrial conduction in the rabbit heart. *J Mol Cell Cardiol* 14: 633–643, 1982.
5. **Boyett MR, Honjo H, Yamamoto M, Nikmaram MR, Niwa R, and Kodama I.** A downward gradient in action potential duration along the conduction path in and around the sinoatrial node. *Am J Physiol Heart Circ Physiol* 276: H686–H698, 1999.
6. **Boyett MR, Honjo H, Yamamoto M, Niwa R, and Kodama I.** Regional differences in the effects of 4-aminopyridine within the sinoatrial node. *Am J Physiol Heart Circ Physiol* 275: H1158–H1168, 1998.
7. **Brahmajothi MV, Morales MJ, Reimer KA, and Strauss HC.** Regional localization of *ERG*, the channel protein responsible for the rapid component of the delayed rectifier, K^+ current in the ferret heart. *Circ Res* 81: 128–135, 1997.
8. **Brown AM, Lee KS, and Powell T.** Sodium current in single rat heart muscle cells. *J Physiol (Lond)* 318: 479–500, 1981.
9. **Brown HF, Kimura J, Noble D, Noble SJ, and Taupignon A.** The ionic currents underlying pacemaker activity in rabbit sino-atrial node: experimental results and computer simulation. *Proc R Soc Lond B Biol Sci* 222: 329–347, 1984.

10. Brown HF, Kimura J, Noble D, Noble SJ, and Taupignon A. The slow inward current, i_{si} , in the rabbit sino-atrial node investigated by voltage clamp and computer simulation. *Proc R Soc Lond B Biol Sci* 222: 305–328, 1984.
11. Colatsky TJ. Voltage clamp measurements of sodium channel properties in rabbit Purkinje fibres. *J Physiol (Lond)* 305: 215–234, 1980.
12. Coppin S, Kodama I, Boyett MR, Dobrzynski H, Takagishi Y, Honjo H, Yeh H-I, and Severs N. Connexin45, a major connexin of the rabbit sinoatrial node, is co-expressed with connexin43 in a restricted zone at the nodal-crista terminalis border. *J Histochem Cytochem* 47: 907–918, 1999.
13. Demir SS, Clark JW, Murphey CR, and Giles WR. A mathematical model of a rabbit sinoatrial node cell. *Am J Physiol Cell Physiol* 266: C832–C852, 1994.
14. Denyer JC and Brown HF. Rabbit sino-atrial node cells: isolation and electrophysiological properties. *J Physiol (Lond)* 428: 405–424, 1990.
15. DiFrancesco D. The contribution of the “pacemaker” current (i_p) to generation of spontaneous activity in rabbit sino-atrial node myocytes. *J Physiol (Lond)* 434: 23–40, 1991.
16. DiFrancesco D, Ferroni A, Mazzanti M, and Tromba C. Properties of the hyperpolarizing-activated current (i_p) in cells isolated from the rabbit sino-atrial node. *J Physiol (Lond)* 377: 61–88, 1986.
17. DiFrancesco D and Noble D. A model of cardiac electrical activity incorporating ionic pumps and concentration changes. *Philos Trans R Soc Lond B Biol Sci* 307: 353–398, 1985.
18. Dokos S, Celler BG, and Lovell NH. Modification of DiFrancesco-Noble equations to simulate the effects of vagal stimulation on in vivo mammalian sinoatrial node electrical activity. *Ann Biomed Eng* 21: 321–335, 1999.
19. Fermini B and Nathan RD. Removal of sialic acid alters both T- and L-type calcium currents in cardiac myocytes. *Am J Physiol Heart Circ Physiol* 260: H735–H743, 1991.
20. Fozzard HA, Haber E, Jennings RB, and Katz AM. *The Heart and the Cardiovascular System*. New York: Raven, 1991.
21. Giles W and van Ginneken ACG. A transient outward current in isolated cells from the crista terminalis of rabbit heart. *J Physiol (Lond)* 368: 243–264, 1985.
22. Hagiwara N, Irisawa H, and Kameyama M. Contribution of two types of calcium currents to the pacemaker potentials of rabbit sino-atrial node cells. *J Physiol (Lond)* 395: 233–253, 1988.
23. Heath BM and Terrar DA. Separation of the components of the delayed rectifier potassium current using selective blockers of i_{Kr} and i_{Ks} in guinea-pig isolated ventricular myocytes. *Exp Physiol* 81: 587–603, 1996.
24. Heath BM and Terrar DA. The deactivation kinetics of the delayed rectifier components i_{Kr} and i_{Ks} in guinea-pig isolated ventricular myocytes. *Exp Physiol* 81: 605–621, 1996.
25. Hilgemann DW and Noble D. Excitation-contraction coupling and extracellular calcium transients in rabbit atrium: reconstruction of basic cellular mechanisms. *Proc R Soc Lond B Biol Sci* 230: 163–205, 1987.
26. Hodgkin AL and Huxley AF. A quantitative description of membrane current and its application to conduction and excitation. *J Physiol (Lond)* 117: 500–557, 1952.
27. Honjo H, Boyett MR, Kodama I, and Toyama J. Correlation between electrical activity and the size of rabbit sinoatrial node cells. *J Physiol (Lond)* 496: 795–808, 1996.
28. Honjo H, Lei M, Boyett MR, and Kodama I. Heterogeneity of 4-aminopyridine-sensitive current in rabbit sinoatrial node cells. *Am J Physiol Heart Circ Physiol* 276: H1295–H1304, 1999.
29. Ito H and Ono K. A rapidly activating delayed rectifier K^+ channel in rabbit sinoatrial node cells. *Am J Physiol Heart Circ Physiol* 269: H443–H452, 1995.
30. Kirchhof CJHJ, Bonke FIM, Allesie MA, and Lammers WJEP. The influence of the atrial myocardium on impulse formation in the rabbit sinus node. *Pflügers Arch* 410: 198–203, 1987.
31. Kodama I and Boyett MR. Regional differences in the electrical activity of the rabbit sinus node. *Pflügers Arch* 404: 214–226, 1985.
32. Kodama I, Boyett MR, Nikmaram MR, Yamamoto M, Honjo H, and Niwa R. Regional differences in the effects of E-4031 within the sinoatrial node. *Am J Physiol Heart Circ Physiol* 276: H793–H802, 1999.
33. Kodama I, Nikmaram MR, Boyett MR, Suzuki R, Honjo H, and Owen JM. Regional differences in the role of the Ca^{2+} and Na^+ currents in pacemaker activity in the sinoatrial node. *Am J Physiol Heart Circ Physiol* 272: H2793–H2806, 1997.
34. Kreitner D. Electrophysiological study of the two main pacemaker mechanisms in the rabbit sinus node. *Cardiovasc Res* 19: 304–318, 1985.
35. Lei M. *Electrophysiological Studies of Rabbit Sino-Atrial Cells* (PhD thesis). Oxford, UK: University of Oxford, 1997.
36. Lei M and Boyett MR. Inhibition of transient outward current, i_{to} , by flecainide and quinidine in rabbit isolated sinoatrial node cells. *J Physiol (Lond)* 511: 78P–79P, 1998.
37. Lei M and Brown HF. Two components of the delayed rectifier potassium current, I_K , in rabbit sino-atrial node cells. *Exp Physiol* 81: 725–741, 1996.
38. Lei M, Brown HF, and Noble D. What role do T-type calcium channels play in cardiac pacemaker activity? In: *Low-Voltage-Activated T-Type Calcium Channels*, edited by Tsien RW, Clozel J-P, and Nargeot J. Chester, UK: Adis International, 1998, p. 103–109.
39. Lei M, Honjo H, and Boyett MR. Characterisation of the transient outward current in rabbit sinoatrial node cells. *Cardiovasc Res*. In press.
40. Li J, Qu J, and Nathan RD. Ionic basis of ryanodine’s negative chronotropic effect on pacemaker cells isolated from the sino-atrial node. *Am J Physiol Heart Circ Physiol* 273: H2481–H2489, 1997.
41. Lindblad DS, Murphey CR, Clark JW, and Giles WR. A model of the action potential and underlying membrane currents in a rabbit atrial cell. *Am J Physiol Heart Circ Physiol* 271: H1666–H1696, 1996.
42. Liu ZW, Zou A-R, Demir SS, Clark JW, and Nathan RD. Characteristics of a hyperpolarisation-activated inward current in cultured pacemaker cells from the sinoatrial node. *J Mol Cell Cardiol* 28: 2523–2535, 1996.
43. Muramatsu H, Zou A-R, Berkowitz GA, and Nathan RD. Characterization of a TTX-sensitive Na^+ current in pacemaker cells isolated from rabbit sinoatrial node. *Am J Physiol Heart Circ Physiol* 270: H2108–H2119, 1996.
44. Nikmaram MR. *Regional Differences in the Regulation of the Rabbit Cardiac Pacemaker* (PhD thesis). Leeds, UK: University of Leeds, 1996.
45. Nikmaram MR, Boyett MR, Kodama I, Suzuki R, and Honjo H. Variation in the effects of Cs^+ , UL-FS 49, and ZD7288 within the sinoatrial node. *Am J Physiol Heart Circ Physiol* 272: H2782–H2792, 1997.
46. Nilius B. Possible functional significance of a novel type of cardiac calcium channel. *Biomed Biochim Acta* 45: K37–K45, 1986.
47. Noble D. A modification of the Hodgkin-Huxley equations applicable to Purkinje fibre action and pacemaker potentials. *J Physiol (Lond)* 160: 317–352, 1962.
48. Noble D. *Oxsoft HEART*, version 4.8. Oxford, UK: Oxsoft, 1990.
49. Noble D and Noble SJ. A model of sino-atrial node electrical activity based on a modification of the DiFrancesco-Noble (1984) equations. *Proc R Soc Lond B Biol Sci* 222: 295–304, 1984.
50. Noble D, Varghese A, Kohl P, and Noble P. Improved guinea-pig ventricular cell model incorporating a diadic space, I_{Kr} and I_{Ks} , and length- and tension-dependent processes. *Can J Cardiol* 14: 123–134, 1998.
51. Ono K and Ito H. Role of rapidly activating delayed rectifier K^+ current in sinoatrial node pacemaker activity. *Am J Physiol Heart Circ Physiol* 269: H453–H462, 1995.
52. Oosthoek PW, Viragh S, Mayen AEM, van Kempen MJA, Lammers WH, and Moorman AFM. Immunohistochemical delineation of the conduction system. I. The sinoatrial node. *Circ Res* 73: 473–481, 1993.
53. Ophhof T. The mammalian sinoatrial node. *Cardiovasc Drugs Ther* 1: 573–597, 1988.

54. **Panfilov AV and Holden AV.** *Computational Biology of the Heart*. Chichester, UK: Wiley, 1997.
55. **Press WH, Flannery BP, Teukolsky SA, and Vetterling WT.** *Numerical Recipes. The Art of Scientific Computing*. Cambridge, UK: Cambridge University Press, 1990.
56. **Shibasaki T.** Conductance and kinetics of delayed rectifier potassium channels in nodal cells of the rabbit heart. *J Physiol (Lond)* 387: 227–250, 1987.
57. **Van Ginneken ACG and Giles W.** Voltage-clamp measurements of the hyperpolarization-activated inward current I_f in single cells from rabbit sino-atrial node. *J Physiol (Lond)* 434: 57–83, 1991.
58. **Verheijck EE, Wessels A, van Ginneken ACG, Bourier J, Markman MWM, Vermeulen JLM, de Bakker JMT, Lamers WH, Opthof T, and Bouman LN.** Distribution of atrial and nodal cells within rabbit sinoatrial node. Models of sinoatrial transition. *Circulation* 97: 1623–1631, 1998.
59. **Wilders R, Jongsma HJ, and van Ginneken ACG.** Pacemaker activity of the rabbit sinoatrial node. A comparison of mathematical models. *Biophys J* 60: 1202–1216, 1991.
60. **Winslow RL, Kimball AL, Varghese A, and Noble D.** Simulating cardiac sinus and atrial network dynamics on the connection machine. *Physica D* 3: 281–298, 1993.
61. **Yanagihara K, Noma A, and Irisawa H.** Reconstruction of sinoatrial node pacemaker potential based on the voltage-clamp experiments. *Jpn J Physiol* 30: 841–857, 1980.
62. **Zaza A, Micheletti M, Brioschi A, and Rocchetti M.** Ionic currents during sustained pacemaker activity in rabbit sino-atrial myocytes. *J Physiol (Lond)* 505: 677–688, 1999.
63. **Zhang H, Boyett MR, Holden AV, Honjo H, and Kodama I.** A computer model of pacemaker shift within the rabbit sino-atrial node (Abstract). *J Physiol (Lond)* 504: 70P, 1997.
64. **Zhang H, Boyett MR, Holden AV, Honjo H, and Kodama I.** A hypothesis to explain the decline of sinoatrial node function with age. *J Physiol (Lond)* 511: 76P–77P, 1998.
65. **Zhang H, Boyett MR, Holden AV, Honjo H, and Kodama I.** Evidence that the Na^+ current, i_{Na^+} , in the periphery of the sinoatrial node helps the node to drive the surrounding atrial muscle. *J Physiol (Lond)* 506: 54P–55P, 1998.
66. **Zhang H, Holden AV, and Boyett MR.** The pacemaking system of the heart: from coupled oscillators to nonlinear waves. *Nonlinear Anal Theory Methods Appl* 30: 1019–1027, 1997.
67. **Zhang H, Holden AV, Kodama I, Honjo H, Lei M, Takagishi Y, and Boyett MR.** Hypothesis to explain the block zone protecting the sinoatrial node (Abstract). *Biophys J* 76: A368, 1999.

